

TOPICAL REVIEW • OPEN ACCESS

Nuts and bolts of 4D-MRI for radiotherapy

To cite this article: B Stemkens *et al* 2018 *Phys. Med. Biol.* **63** 21TR01

View the [article online](#) for updates and enhancements.

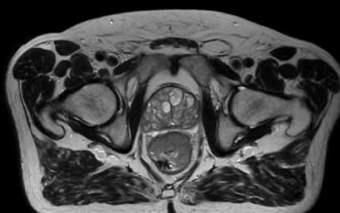
Recent citations

- [A ROI-based global motion model established on 4DCT and 2D cine-MRI data for MRI-guidance in radiation therapy](#)
Noemi Garau *et al*

Uncompromised.

See clearly during treatment to attack the tumor and protect the patient.

Two worlds, one future.



Captured on Elekta high-field MR-linac during 2018 imaging studies.

 **Elekta**

Elekta MR-linac is pending 510(k) premarket clearance and not available for commercial distribution or sale in the U.S.

OPEN ACCESS

TOPICAL REVIEW



Nuts and bolts of 4D-MRI for radiotherapy

RECEIVED
21 May 2018REVISED
5 September 2018ACCEPTED FOR PUBLICATION
1 October 2018PUBLISHED
23 October 2018

Original content from this work may be used under the terms of the [Creative Commons Attribution 3.0 licence](#).

Any further distribution of this work must maintain attribution to the author(s) and the title of the work, journal citation and DOI.

B Stemkens^{1,2}, E S Paulson^{3,4,5} and R H N Tijssen¹¹ Department of Radiotherapy, University Medical Center Utrecht, Heidelberglaan 100, 3584 CX Utrecht, Netherlands² MR Code B.V., Schimminck 18, 5301 KR Zaltbommel, Netherlands³ Departments of Radiation Oncology, Medical College of Wisconsin, Milwaukee, WI, United States of America⁴ Departments of Radiology, Medical College of Wisconsin, Milwaukee, WI, United States of America⁵ Departments of Biophysics, Medical College of Wisconsin, Milwaukee, WI, United States of AmericaE-mail: b.stemkens@umcutrecht.nl**Keywords:** 4D-MRI, magnetic resonance imaging, MRI-guided radiotherapy, motion, abdomen, thorax, respiratory-correlatedSupplementary material for this article is available [online](#)**Abstract**

Magnetic resonance imaging (MRI) is increasingly being used in the radiotherapy workflow because of its superior soft tissue contrast and high flexibility in contrast. In addition to anatomical and functional imaging, MRI can also be used to characterize the physiologically induced motion of both the tumor and organs-at-risk. Respiratory-correlated 4D-MRI has gained large interest as an alternative to 4D-CT for the characterization of respiratory motion throughout the thorax and abdomen. These 4D-MRI data sets consist of three spatial dimensions and the respiratory phase or amplitude over the fourth dimension (opposed to time-resolved 4D-MRI that represents time in the fourth dimension). Over the last 15 years numerous methods have been presented in literature. This review article provides a comprehensive overview of the various 4D-MRI techniques, and describes the differences in MRI data acquisition and 4D data set generation from a methodological point of view. The current status and future perspective of these techniques are highlighted, and the requirements for safe introduction into the clinic (e.g. method validation) are discussed.

1. Introduction

The use of magnetic resonance imaging (MRI) in radiation therapy has increased dramatically over the past decade (Ménard and van der Heide 2014). Its ability to generate both anatomical and functional contrast and its high flexibility in image acquisition strategy allows clear distinction between tumorous tissue and organs at risk (OARs). This aids the delineation process, informs about functional parameters, and can be used to assess treatment response (Dirix *et al* 2014). Besides anatomical imaging, such as T₁ and T₂-weighted imaging, functional imaging, such as diffusion weighted imaging (DWI) and dynamic contrast enhanced (DCE) imaging, has been used successfully to discriminate between healthy and tumorous tissue (e.g. Pickles *et al* (2006) and van der Heide *et al* (2012)).

In addition to delineation, tumor motion can be characterized through MR imaging for tumors that move due to physiological processes, such as respiration, cardiac pulsatile motion, or peristaltic motion. Respiration, which is the prime focus in this review article, induces quasi-periodic tumor displacements (i.e. a periodic motion trajectory with a small unpredictable component). Respiratory-induced displacements can be up to several centimeters in cranio-caudal (CC) direction (Von Siebenthal *et al* 2007, Heerkens *et al* 2014). Hence, respiration is the main source of motion for abdominothoracic tumors. It is therefore important to characterize the respiratory-induced motion of the tumor and OARs in order to minimize radiation toxicity to healthy tissue and maximize radiation to the tumor during radiotherapy. While this is traditionally carried out using 4D computed tomography (CT), 4D-MRI can similarly be used to provide this fundamental motion information for treatment planning. This motion information can then be used for (personalized) internal target volume (ITV) margins (International Commission on Radiation Units and Measurements 1999), the generation of mid-ventilation (Wolthaus *et al* 2006) or mid-position (Wolthaus *et al* 2008a) volumes that approximate or represent the time-averaged anatomy, or be taken into account through 4D planning strategies (Unkelbach and Oelfke 2004). However, opposed to 4D-CT, 4D-MRI can visualize the underlying anatomy in any desired orientation,

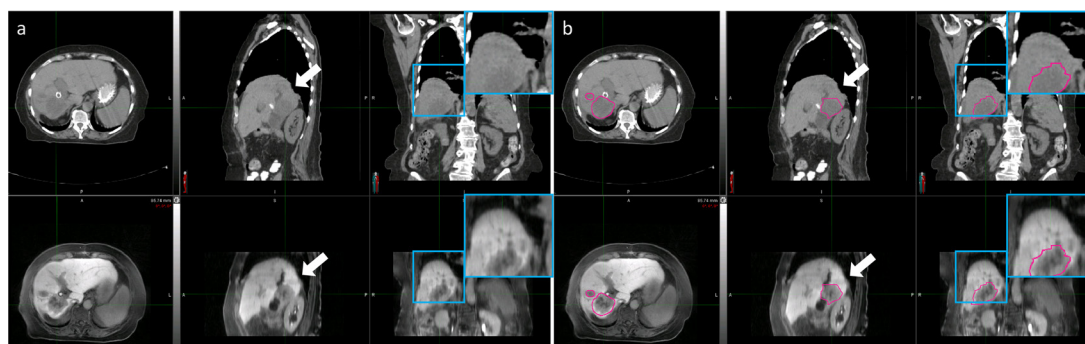


Figure 1. 4D-CT, 4D-MRI comparison. Comparison of inspiratory phase 4D-CT (top) and 4D-MRI (bottom) in a cholangiocarcinoma patient. The 4D-MRI was acquired with a 3D golden-angle radial stack-of-stars sequence and reconstructed using the XD-GRASP (extra-dimensional golden-angle radial sparse parallel imaging) algorithm. Compared to 4D-CT, 4D-MRI demonstrates increased soft-tissue contrast for gross tumor volume delineation in pink (a), (b) and reduced stitching artifacts (white arrow) compared to 4D-CT, which is also observed in the zoomed images (blue rectangle).

since 4D-CT only allows for transversal imaging, the imaging orientation in 4D-MRI can be chosen at will. Furthermore 4D-MRI does not use ionizing radiation, which may be especially beneficial for pediatric patients. Moreover, 4D-MRI can picture both tumor and OARs, which is often difficult in 4D-CT, due to its limited soft-tissue contrast (see figure 1 and supplementary video 1 (stacks.iop.org/PMB/63/21TR01/mmedia)). Unfortunately, 4D-MRI cannot readily be generated on a clinical MRI system, since currently none of the major MR vendors offer 4D-MRI as product implementation. To fill this gap, a considerable number of 4D-MRI methods have been published in the literature over the past 15 years. In general, these implementations acquire MR data over a longer period of time, to sample sufficient respiratory cycles, in combination with a respiratory surrogate signal that is used to sort the data into different respiratory phases or displacements.

This review focuses on 4D-MRI implementations for radiotherapy planning and treatment. Throughout this review, the term 4D-MRI refers to *respiratory-correlated* 4D-MRI, unless otherwise specified. In a respiratory-correlated 4D-MRI the four dimensions indicate the three spatial dimensions and the *respiratory phase*. This is different from *time-resolved* 4D-MRI, where the fourth dimension is represented by *time*. In our search for 4D-MRI implementations for radiotherapy, we have found a total of 61 papers describing different techniques and focusing on different aspects of the implementation (up through March 2018). Especially over the last three years, a large increase in the number of papers describing different 4D-MRI techniques was observed (see table 1 at the end of this review). To put all these techniques into perspective, the review will categorize these techniques and describe the different considerations that have to be made when implementing 4D-MRI.

The main focus of this review is to:

- (1) Provide a detailed analysis of the intricacies of the MR physics behind the various acquisition and reconstruction strategies that are currently proposed for 4D-MRI generation.
- (2) Describe and categorize the different 4D-MRI acquisitions published in literature.
- (3) Highlight potential pitfalls for the acquisition and reconstruction of a 4D-MRI data set.
- (4) Provide an outlook on future research and developments in the field of 4D-MRI.

This review is divided into different sections. First, basic MR theory is described to understand the different implementations that are published. The second part focuses on the different acquisition strategies that are used throughout literature and how respiratory surrogate signals, which are required to generate a respiratory-correlated 4D-MRI data set, are extracted. Next, the generation of such respiratory-correlated 4D-MRI data sets is described alongside the validation of the generated data sets. Finally, the clinical applications are discussed and an outlook is included where developments and future research are described.

2. MR signal theory

MRI physics is often considered challenging and more complex than other imaging modalities. Here, we will briefly introduce some of the basic principles of MR Image formation that are required to understand the methods described in the remainder of this paper. For a more comprehensive background, including signal formation fundamentals, the reader is referred to the excellent textbooks by Haacke *et al* (1999) and Bernstein *et al* (2004), in particular chapters 1, 4, 10, 14, 15, and 11, 13, 14, 17, respectively. Concepts like spin polarization, excitation, and signal detection are assumed to be known to the reader and are not covered here for conciseness. MRI experts may choose to skip this section.

Table 1. Overview of the different 4D-MRI implementations published in literature. n/a = information not available; cine = first acquire all dynamics for one slice, then move on to next slice; sequential = first all slices for one dynamic, repeat for N dynamics; continuous = continuous scanning (mostly for 3D); bSSFP = balanced steady-state free precession; SPGR = Spoiled gradient echo; FLASH = fast low angle shot; T₂-TSE = T₂-turbo spin echo; HASTE = Half-Fourier acquisition single-shot turbo spin echo; GRE = gradient echo; methods that do not use a surrogate and are lacking a sorting domain are time-resolved 4D acquisition (generally low spatial resolution and/or coverage).

Authors	Region	Surrogate	Acquisition type	Sorting domain	Readout order	Contrast	Field Strength	Resolution	Field-of-view	Acquisition time
Rohlfing <i>et al</i> (2004)	Liver	Respiratory bellows	2D Cartesian transversal	Image space	Prospective	T ₂ -TSE	1.5T GE	1.56 × 1.56 mm ² , 5 mm	400 × 400 mm ² , 192 mm	n/a
Plathow <i>et al</i> (2005)	Lung	—	3D Cartesian transversal	—	Continuous	bSSFP	1.5T Siemens	3.75 × 3.75 × 3.8 mm ³	375 × 400 × 198 mm ³	20 s
von Siebenthal <i>et al</i> (2005)	Liver	2D interleaved navigator	2D Cartesian sagittal	Image space	Cine	bSSFP	1.5T Philips	1.8 × 1.8 mm ² , 3.0 mm	345 × 345 mm ² , 90 mm	30 min
Plathow <i>et al</i> (2006)	Pulmonary nodes	—	3D Cartesian transversal	—	Continuous	FLASH	1.5T Siemens	3.75 × 3.75 × 3.8 mm ³	375 × 400 × 198 mm ³	~20 s
Blackall <i>et al</i> (2006)	Lung	Breath holds	2D Cartesian sagittal	Image space	Continuous	bSSFP	1.5T Philips	1.1–1.8 × 1.1–1.8 mm ² , 6 mm	450 × 450 mm ² , 150 mm	n/a
Kauczor and Plathow (2006)	Lung	—	3D Cartesian transversal	—	Continuous	bSSFP	1.5T Siemens	3.0 × 3.0 × 3.0 mm ³	375 × 400 × 198 mm ³	n/a
Von Siebenthal <i>et al</i> (2007)	Liver/lung	2D interleaved navigator	2D sagittal	Image space	Cine	bSSFP	1.5T Philips	1.8 × 1.8 mm ² , 3–4 mm	345 × 345 mm ² , 100 mm	60 min
Remmert <i>et al</i> (2007)	Porcine lung	Optical tracking	2D Cartesian coronal + transversal	Image space	Sequential	FLASH	1.5T Siemens	2.7 × 2.7 mm ² , 10 mm	350 × 350 mm ² , 250 mm	160 s
Tokuda <i>et al</i> (2008)	Liver	1D navigator	2D Cartesian transversal and sagittal	Image space	Prospective	FISP	0.5T GE	1.2 × 2.3 mm ² , 7 mm	300 × 300 mm ² , 120–167 mm	8–22 min
Dinkel <i>et al</i> (2009)	Lung	—	3D Cartesian coronal	—	Continuous	SPGR	1.5T Siemens	3.1 × 3.1 × 4.0 mm ³	400 × 300 × ?? mm ³	n/a
Masuda and Haneishi (2010)	Lung	2D navigator	2D Coronal	Image space	Cine	bSSFP	1.5T Philips	1.5 × 1.5 mm ² , 7.5 mm	384 × 384 mm ² , ??mm	30 min
Cai <i>et al</i> (2011)	Liver/lung	Body area	2D Transversal	Image space	Cine	bSSFP	1.5T Siemens	1.5 × 1.5 mm ² , 5 mm	350 × 227 mm ² , ??mm	n/a
Arnold <i>et al</i> (2011)	Liver	1D navigator	2D sagittal	Image space	n/a	n/a	n/a	1.4 × 1.4 mm ² , 4 mm	?? × ?? × 100–120 mm	14–26 min
Buerger <i>et al</i> (2012)	Liver	Self-navigation	3D Golden radial phase encoding	k -space	Continuous	bSSFP	1.5T Philips	1.75 × 1.75 × 1.75 mm ³	287 × 287 × 287 mm ³	6 min 47 s
Boye <i>et al</i> (2013)	Liver	2D interleaved navigator	2D sagittal	Image space	Cine	bSSFP	1.5T Philips	1.8 × 1.8 mm ² , 4 mm	345 × 345 mm ² , 100 mm	60 min
Tryggstad <i>et al</i> (2013)	Liver/lung	Respiratory bellows	2D Sagittal and coronal	Image space	Sequential	bSSFP/HASTE	1.5T Siemens	2.0 × 2.0 mm ² , 5 mm	330 × 330 mm ² , 75–150 mm	8–30 min
Hu <i>et al</i> (2013)	Liver	Respiratory bellows	2D Transversal and sagittal	Image space	Propsective	T ₂ -TSE	1.5T Philips	1.5 × 1.5 mm ² , 5 mm	375 × 264 mm ² , 160 mm	3 min
Marx <i>et al</i> (2014)	Lung	DIR	3D Cartesian Transversal	—	Continuous	GRE	1.5 Siemens	3.91 × 3.91 × 3.91 mm ³	500 × 360 × 500 mm ³	1 min 20 s

(Continued)

Table 1. (Continued)

Authors	Region	Surrogate	Acquisition type	Sorting domain	Readout order	Contrast	Field Strength	Resolution	Field-of-view	Acquisition time
Swastika <i>et al</i> (2013)	Lung	Diaphragm displacement	2D Coronal	Image space	Cine	bSSFP	1.5T Philips	1.5 × 1.5 mm ² , 7.5 mm	384 × 384 mm ² , 120–180 mm	12–24 min
Würslin <i>et al</i> (2013)	Lung/ abdomen	Navigator	2D Sagittal	Image space	Cine	SPGR	3.0T Siemens	2.0 × 2.0 mm ² , 10 mm	384 × 288 mm ² , 360 mm	3 min
Celicanin <i>et al</i> (2013)	Liver	2D Navigator (CAIPIRINHA)	2D Sagittal	Image space	Sequential	bSSFP	1.5T Siemens	1.9 × 1.9 mm ² , 6 mm	225 × 240 mm ² , 120 mm	60 min
Tanner <i>et al</i> (2014)	Liver	2D interleaved navigator	2D Sagittal	Image space	Cine	bSSFP	1.5T Philips	1.3 × 1.3 mm ² , 5 mm	224 × 240 mm ² , 224–240 mm	9–12 min
Tong <i>et al</i> (2014)	Lung	Graph-based	2D Coronal or sagittal	Image space	Cine	bSSFP	n/a	0.98–2.21 × 0.98–2.21 mm ² , 3.6–6.0 mm	n/a	n/a
Liu <i>et al</i> (2014)	Liver	Body area	2D Sagittal	Image space	Cine	bSSFP	1.5T GE	1.9 × 1.9 mm ² , 5 mm	480 × 480 mm ² ,	n/a
Yang <i>et al</i> (2014)	Liver	Body area	2D Transversal	Image space	Cine	bSSFP	1.5T GE / 3.0T Siemens	1.6–2.5 × 2.8–3.75 mm ² , 5.0 mm	300–480 × 360–480 mm ² , ??mm	n/a
Stemkens <i>et al</i> (2015)	Pancreas	1D Navigator	3D Radial stack-of-stars Transversal	<i>K</i> -space	Consecutive	bSSFP	1.5T Philips	2.0 × 2.0 × 4.0 mm ³	330 × 330 × 96 mm ³	8 min 35 s
Cai <i>et al</i> (2015)	Liver	Fourier phase	2D Coronal or sagittal	Image space	Cine	bSSFP	1.5T Siemens	2.3 × 2.3 mm ² , 7.0 mm	300 × 260 mm ² , 7 mm	5 min
Yang <i>et al</i> (2015d)	Lung	—	3D Cartesian Transversal	—	Continuous	SPGR	3.0T Siemens	2.81 × 2.81 × 4 mm ³	360 × 360 × 144 mm ³	n/a
Yue <i>et al</i> (2015a)	Phantom	Self-gating	3D Radial	<i>k</i> -space	Continuous	SPGR	3.0T Siemens	1.56 × 1.56 × 1.56 mm ³	300 × 300 × 300 mm ³	8 min
Liu <i>et al</i> (2015a)	Liver / Lung	Respiratory bellows	2D transversal	Image space	Sequential	T ₂ -TSE	3.0T Siemens	1.4 × 1.4 mm ² , 5.0 mm	350 × 317 mm ² , 75–165 mm	n/a
Du <i>et al</i> (2015)	Liver	Respiratory bellows	2D sagittal	Image space	Prospective	T ₂ -TSE	1.5T Philips	1.5 × 1.5 mm ² , 3.0 mm	375 × 260 mm ² , 180 mm	9–18 min
Yang <i>et al</i> (2015b)	Pancreas	Self-navigation	3D Radial	<i>k</i> -space	Continuous	SPGR	3.0T Siemens	1.56 × 1.56 × 1.56 mm ³	300 × 300 × 300 mm ³	8 min
Paganelli <i>et al</i> (2015)	Liver	Mutual Information	2D Transversal	Image space	Sequential	bSSFP	1.5T Siemens	1.28 × 1.28 mm ² , 5.0 mm	320 × 285 mm ² , 100 mm	72 s
Glide-Hurst <i>et al</i> (2015)	Liver	Respiratory bellows	2D Sagittal	Image space	Prospective	T ₂ -TSE	1.0T Philips	1.0 × 1.0 mm ² , 4.0 mm	380 × 210 mm ² , 200 mm	8–17 min
Liu <i>et al</i> (2015b)	Liver / lung	Respiratory bellows	2D Transversal	<i>K</i> -space	Sequential	T ₂ -TSE	3.0T GE	1.56 × 1.56 mm, 8.0 mm	400 × 400 mm ² , 72 mm	2 min 20 s
Deng <i>et al</i> (2016)	Liver	Self-navigation	3D Radial	<i>k</i> -space	Continuous	SPGR	3.0T Siemens	1.56 × 1.56 × 1.56 mm ³	300 × 300 × 300 mm ³	8 min
Liang <i>et al</i> (2016)	XCAT phantom	n/a	n/a	n/a	n/a	n/a	n/a	1.0 × 1.0 mm ² , 5 mm	512 × 512 mm ² , 250 mm	n/a
Uh <i>et al</i> (2016)	Liver / Lung	Diaphragm navigator	2D Coronal	Image space	Cine	bSSFP	1.5T Siemens	1.8 × 1.8 mm ² , 5 mm	350 × 350 mm ² , 100 mm	8 min 12 s

(Continued)

Table 1. (Continued)

Authors	Region	Surrogate	Acquisition type	Sorting domain	Readout order	Contrast	Field Strength	Resolution	Field-of-view	Acquisition time
Hui <i>et al</i> (2016)	Liver	Fourier signals	2D Sagittal	Image space	Cine	bSSFP	1.5T Philips	2.0 × 2.0 mm ² , 5.0 mm	400 × 200 mm ² , 300 mm	30 min
Liu <i>et al</i> (2016)	XCAT	—	2D Transversal	Image space	Cine/sequential	T ₂ -TSE	—	n/a	n/a	4–5 min
Rank <i>et al</i> (2016a)	Lung	Self-navigation	3D Radial stack-of-stars sagittal	<i>k</i> -space	Continuous	SPGR	3.0T Siemens	1.6 × 1.6 × 4.5 mm ³	400 × 400 × 396 mm ³	5 min
Bernatowicz <i>et al</i> (2016)	Liver	2D Interleaved navigator	2D Sagittal	Image space	Cine	bSSFP	n/a	1.8 × 1.8 mm ² , 3–4 mm	345 × 345 mm ² , ??mm	60 min
To <i>et al</i> (2016)	Liver	Respiratory bellows	2D Coronal	Image space	Prospective	T ₂ -TSE	1.0T Philips	0.98 × 0.98 mm ² , 4.0–5.0 mm	450 × 450 mm ² , 210–245 mm	5–10 min
Harris <i>et al</i> (2016)	Liver	Body area	2D Transversal or sagittal	Image space	Cine	bSSFP	1.5T GE	1.9 × 1.9 mm ² , 5.0 mm	480 × 480 mm ² , ??mm	n/a
Stemkens <i>et al</i> (2016b)	Pancreas/kidney	1D Navigator	3D Radial stack-of-stars Transversal	<i>k</i> -space	Continuous	bSSFP	1.5T Philips	1.9 × 1.9 × 4.0 mm ³	330 × 330 × 132 mm ³	8 min 35 s
Rank <i>et al</i> (2017)	Lung/abdomen	Self-navigation	3D radial stack-of-stars Coronal or Sagittal	<i>k</i> -space	Continuous	SPGR	1.5T Siemens	1.5 × 1.5 × 5.0 mm ³	385 × 385 × 300 mm ³	37–41 s
Mickevicius and Paulson (2017)	Abdomen	Self-navigation	3D radial stack-of-stars Transversal	<i>k</i> -space	Continuous	SPGR	3.0T Siemens	1.8–3.0 × 1.8–3.0 × 6.0 mm ³	330 × 330 × 240 mm ³	120–142 s
Küstner <i>et al</i> (2017)	Lung/abdomen	Self-navigation	3D Cartesian	<i>k</i> -space	Continuous	SPGR	3.0T Siemens	1.95 × 1.95 × 5 mm ³	500 × 500 × 360 mm ³	6 min 23 s
Uh <i>et al</i> (2017)	Abdomen	Diaphragm displacement	2D Coronal	Image space	Cine	bSSFP	1.5/3.0T Siemens	1.8 × 1.8 mm ² , 4–5 mm	350 × 350 mm ² , 140 mm	11–20 min
Li <i>et al</i> (2017)	Abdomen	Respiratory bellows or 1D navigator	2D Coronal or sagittal	Image space	Prospective	T ₂ -TSE	3.0T Philips	2.0 × 2.0 mm ² , 5 mm	370 × 240 mm ² , 420 mm	8–12 min
Liu <i>et al</i> (2017b)	Abdomen	Respiratory bellows	2D Transversal	Image space	Sequential	DWI-EPI	3.0T Siemens	3.0 × 3.0 mm ² , 5.0 mm	380 × 285 mm ² , ??mm	5–10 min
Freedman <i>et al</i> (2017)	Abdomen	Self-navigation	3D Radial stack-of-stars Transversal	<i>k</i> -space	Continuous	SPGR	1.5T Siemens	1.3–1.5 × 1.3–1.5 × 3.0–3.3 mm ³	336–384 × 336–384 × 288 mm ³	5–8 min
Han <i>et al</i> (2017)	Abdomen	Self-navigation	3D Cartesian Transversal	<i>k</i> -space	Continuous	bSSFP	1.5T Siemens	1.2 × 1.2 × 1.6 mm ³	500 × 300 × 200 mm ³	5 min
Stemkens <i>et al</i> (2017b)	Kidney	Self-navigation	3D Radial stack-of-stars Transversal	<i>k</i> -space	Continuous	bSSFP	1.5T Philips	1.9 × 1.9 × 2.0 mm ³	300–350 × 300–350 × 132–200 mm ³	3 min 22 s–5 min 03 s
Tong <i>et al</i> (2017)	Lung	Graph-based optimization	2D Coronal / sagittal	Image space	Cine	T2w scan	n/a	0.7–2.2 × 0.7–2.2 mm ² , 2.3–5.0 mm	140–420 × 140–420 mm ² , 70–200 mm	200–1000 s

(Continued)

Table 1. (Continued)

Authors	Region	Surrogate	Acquisition type	Sorting domain	Readout order	Contrast	Field Strength	Resolution	Field-of-view	Acquisition time
Fayad <i>et al</i> (2017)	Lung/abdomen	Diaphragm displacement	2D Sagittal	Image space	Cine	SPGR	3.0T Siemens	$2.0 \times 2.0 \text{ mm}^2$, 10 mm	n/a	180 s
Deng <i>et al</i> (2017)	Abdomen	Self-navigation	3D Radial	<i>k</i> -space	Continuous	SPGR	3.0T Siemens	$1.6 \times 1.6 \times 1.6 \text{ mm}^3$	$400 \times 400 \times 400 \text{ mm}^3$	7 min 23 s
Liu <i>et al</i> (2017a)	Liver	Diaphragm motion	2D coronal	Image space	Cine	bSSFP	1.5T GE / 3.0T Siemens	$1.17 \times 1.17 \text{ mm}^2$, 5 mm	$300 \times 300 \text{ mm}^2$, n/a mm	n/a
Harris <i>et al</i> (2018)	Liver	Body area	2D Transversal/sagittal	Image space	Cine	bSSFP	1.5T GE	$1.9 \times 1.9 \text{ mm}^2$, 5 mm	$480 \times 480 \text{ mm}^2$, n/a mm	n/a
Park <i>et al</i> (2018)	Lung	Body area and group wise registration	2D sagittal	Image space	Sequential	bSSFP	1.5T Siemens	$2.0 \times 2.0 \text{ mm}^2$, 5 mm	$?? \times ?? \text{ mm}^2$, 50–75 mm	5 min
Breuer <i>et al</i> (2018)	Thorax/abdomen	Self-navigation	3D Cartesian coronal	<i>k</i> -space	Continuous	FLASH	1.5T Siemens	$2.1 \times 2.1 \times 2.1 \text{ mm}^3$	$400 \times 400 \times 185 \text{ mm}^3$	5 min 36 s

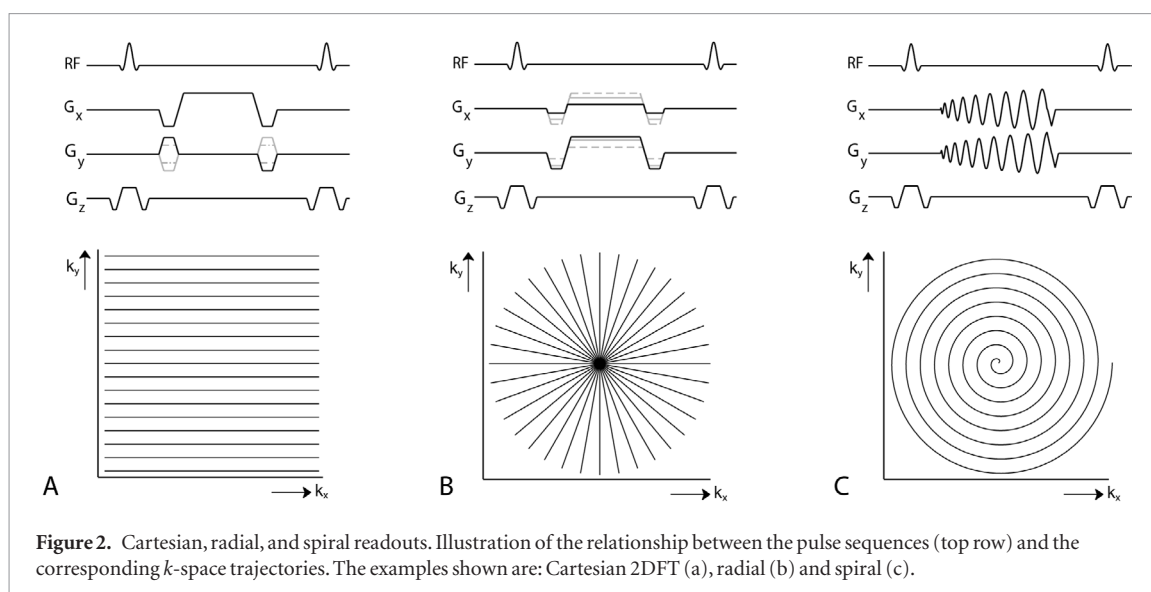


Figure 2. Cartesian, radial, and spiral readouts. Illustration of the relationship between the pulse sequences (top row) and the corresponding k -space trajectories. The examples shown are: Cartesian 2DFT (a), radial (b) and spiral (c).

In MRI, spatial encoding is different from most other imaging modalities as image formation happens in the physical (spatial) and frequency (Fourier) domain. After a spatially selective radiofrequency (RF) pulse the encoding is performed using the ‘field gradients’ of the MRI scanner, which introduce a spatially varying magnetic field. In effect, these field gradients allow local manipulation of the Larmor frequency of the hydrogen spins, which links the spatial encoding to the frequency domain.

2.1. Selective excitation

The process of image formation starts with a selective excitation RF pulse that restricts the excitation to a 2D plane or slab of interest within the patient. A selective excitation is achieved by applying a field gradient *during* the excitation pulse. This creates a range of resonance frequencies along the axis of the applied gradient. Since the excitation is only effective within the frequency band of the RF pulse, the excitation is restricted to the area in which the resonance frequency and RF frequency match. As a result, signal can only originate from this area. The gradient strength in combination with the frequency bandwidth of the RF pulse determines the thickness of the excited slice or slab. By changing the center frequency of the RF pulse one can alter the location of the excited slice along the applied gradient.

2.2. In-plane localization

Once the slice (or slab) is excited, spatial encoding along the remaining dimensions is performed to form an image. Again, the field gradients are used. By applying a linear field gradient the resonance frequency is varied linearly along that particular dimension. This introduces a phase difference between spins at different locations. The amount of phase dispersion is dependent on the amplitude and the duration of the gradient (i.e. the time-integral of the gradient pulse). Since the MR signal is the sum of the entire spin ensemble, the detected signal is actually a measure of phase interference between spins at various spatial frequencies. The native domain, in which the signal is acquired, is therefore the spatial frequency domain, called k -space, where the k -number denotes the spatial frequency. Intuitively, the center of k -space encodes the low spatial frequencies (i.e. sharpens the anatomical structures) and holds information of spatially localized motion. In Cartesian imaging, the lines in k -space are acquired along a rectilinear grid. According to the Nyquist theorem the extent of k -space determines the resolution (Δx) of the image, whereas the distance between the k -space samples (Δk) determines the field-of-view (FOV). Once all k -lines are collected a simple 2D Fourier transform (2DFT) provides the reconstructed image.

2.3. 2D versus 3D acquisitions

In order to collect volumetric imaging data one could repeat the process described above for multiple slice locations. For each slice the location is adjusted by changing the center frequency of the RF pulse. In theory one is free to choose the order in which the slices are collected in, but on most scanners the ordering is limited to sequential (one after another, in subsequent order: 1,2,3,..., n) or interleaved (first the even slices, followed by the odd slices: 2, 4, 6,..., n , 1, 2, 3 ..., $n - 1$). Normally interleaved would be preferred to mitigate slice crosstalk caused by the imperfect slice excitation profile: due to imperfections in the slice excitation pulse, the slice excitation profile is never a perfect block pulse, but rather a rounded shape (i.e. a block pulse convolved by a Gaussian with a certain full width half maximum). As a result a portion of the spins experience excitation twice when

adjacent slices are excited directly after one another. Interleaved scanning allows more time for relaxation before the adjacent slice is excited, thereby mitigating the effect of cross-talk. The thinner the slice, the more difficult it is to produce a rectangular slice profile. Moreover, signal-to-noise ratio (SNR) is linearly dependent on the slice thickness, where thinner slices produce lower SNR. Hence, the slice thickness in 2D multi-slice imaging is usually limited to 3–4 mm.

A solution that overcomes the problem of slice profile imperfections is to acquire a 3D volume instead of multiple 2D slices. In 3D acquisitions the entire volume (i.e. a thick slab) is excited with every RF pulse and a second phase encode axis is used to encode the third dimension. Effectively the slice encoding is thus replaced by Fourier encoding. The advantage of 3D versus 2D acquisitions is that 3D imaging allows isotropic high-resolution imaging, since the slice thickness is not limited by the slice excitation profile. Because the entire volume is excited with every RF pulse (and hence is contributing to the signal) the signal-to-noise (SNR) ratio is typically higher for an equivalent slice thickness. The disadvantage of 3D acquisitions is that the repetition time (T_R) is typically short, which may be limiting in terms of the contrast that is produced. Also, a 3D readout is longer than a 2D readout, so motion *during* image acquisition is more problematic when unaccounted for.

2.4. Cartesian versus non-Cartesian readout trajectories

During the acquisition, k -space is sampled via a path defined by the applied gradients. There are many trajectories possible. The appearance of the image is to a large extent determined by the design of the trajectory. In particular the vulnerability to image artifacts is strongly influenced by the readout trajectory.

Most clinical exams, sample k -space along a Cartesian trajectory: a single gradient, say G_x , is applied, which samples the points in a straight line along the k_x dimension (figure 2(a)). For each line, the phase encode gradient (G_y) moves the trajectory to a different k_y position. A Cartesian readout is a very robust acquisition scheme, since errors in gradient timing, off-resonance effects, or other imperfections only have an effect along a single direction in k -space. The artifacts are therefore either small or predictable. This is the main reason why Cartesian readouts are often the method of choice in clinical exams. A disadvantage of Cartesian imaging is the fact that it produces strong, coherent, aliasing artifacts when the sampled data does not fulfill the Nyquist criteria (i.e. when the acquisition is undersampled), although to a certain extent this can be overcome by the use of parallel imaging techniques, such as SENSitivity Encoding (SENSE) and Generalized Autocalibrating Partially Parallel Acquisitions (GRAPPA) (Pruessmann *et al* 1999, Griswold *et al* 2002) (see section 2.5 for more details).

Non-Cartesian readouts are defined as readouts that do not follow the Cartesian grid. By applying a combination of gradients any path through k -space can be traversed. Examples that are offered by most vendors are radial and spiral figures 2(b) and (c). Non-Cartesian readouts are often used to overcome some of the limitations of Cartesian imaging. Radial readouts, for example, have the advantage that the center of k -space is sampled by every readout line, which makes it very robust against intraview motion (i.e. motion during acquisition). Spiral readouts provide very efficient k -space coverage and make optimal use of the gradient performance. Spiral readouts are therefore often used for fast imaging, such as real-time cardiac MRI (Yang *et al* 1998, Nayak *et al* 2005). Another benefit of non-Cartesian imaging is the fact that undersampling artifacts are incoherent in imaging space, which is beneficial for iterative reconstruction techniques, like compressed sensing that allow higher acceleration factors ($R > 8$) compared to the traditional parallel imaging techniques ($R < 5$) by acquiring less data points.

2.5. Image acceleration

Most 4D-MRI methods described in literature use standard acceleration methods such as partial Fourier (PF) and parallel imaging to reduce scan time. In PF acquisitions a portion of k -space is deliberately not collected (often up to 3/8 or 7/16 of k -space). PF methods rely on the property of the Fourier transform that real functions have conjugate symmetry in k -space. The simplest PF reconstruction fills the missing lines with zeros, although this inherently results in considerable blurring in image space. Other methods synthesize the uncollected lines in k -space by exploiting conjugate phase symmetry in k -space. The assumption of conjugate phase symmetry, however, is only valid when the imaged object is real. In most cases, however, the object has a non-constant phase across the image. Most PF methods that synthesize the missing data in k -space therefore contain some form of phase correction based on the portion of the data that is symmetrically acquired around $k = 0$. The minimum amount of acquired data is therefore slightly more than 50% for 1D PF (typically around 65%). Higher acceleration factors can be achieved with parallel imaging. Parallel imaging methods use the spatially varying coil sensitivity profiles in multi-channel receiver coil arrays to subsample k -space (for example by skipping every other line) (Roemer *et al* 1990, Sodickson and Manning 1997, Pruessmann *et al* 1999, Griswold *et al* 2002). Various accelerated parallel imaging reconstructions have been proposed that either work in the image domain or in k -space. SENSE (Pruessmann *et al* 1999) operates in the image domain: normally skipping every other line in an acquisition would result in an aliased image. SENSE uses the fact that as long as the acquisition is subsampled with equidistant spacing the signal will alias in well-defined locations. The aliased signal in the

acquired images can therefore be written as the sum of the signal from known locations in the unaliased image weighted by the coil sensitivities at these locations. Solving for this set of equations provides the de-aliased image. For this the coil sensitivity information is required, which is usually acquired in a separate scan. The k -space counterpart of SENSE is GRAPPA (Griswold *et al* 2002). GRAPPA aims to fill in the missing data lines in k -space before the data is Fourier transformed into image space. The assumption that is made is that each point in k -space can be synthesized by a linear combination of neighboring data points in the other coil images as long as their coil profiles are sufficiently different. This can be understood by considering that the signal in the image domain is modulated by the coil profile. The effect of this is identical to a convolution in k -space. Each coil therefore effectively samples a slightly shifted line in k -space, which implies that more than one k -space line could be reconstructed from the data if one knew the relationship between the different coils. GRAPPA works by finding the linear coefficients (weights) between the coils necessary to effectively deconvolve the coil profiles and reconstruct multiple lines from different coil signals. The different weights between the target points (the missing points in k -space) and the source points (the acquired neighboring data) are estimated by a reference scan, called the auto-calibration scan (ACS). This can either be a fully sampled central portion of the (undersampled) k -space or a separately acquired reference scan. The relationship between the target points is independent of the location in k -space, and therefore the weights that are estimated from the center of k -space can be applied to the missing data points throughout the rest of k -space. The amount of acceleration depends on the coil geometry and undersampling pattern. In general higher acceleration factors can be achieved for 3D acquisitions, as the undersampling (and thus resulting aliasing) can be divided over two dimensions. Typical acceleration factors for current clinically available multi-channel (e.g. 32 channels) arrays range between $R = 3$ for 2D and $R = 6$ (2×3) for 3D acquisitions. A more recent development is compressed sensing (CS) (Lustig *et al* 2007). CS MRI is an approach to image acceleration that is founded on the notion that all medical images can be compressed by finding an appropriate transform domain, in which the image can be sparsely represented (e.g. spatial finite differences or wavelet domain). This, together with a random sampling pattern in k -space allows images to be reconstructed from far fewer data than prescribed by the Nyquist–Shannon sampling theorem (Liu and Saloner 2014). CS has allowed up to 20-fold image acceleration, far higher than any parallel imaging technique (Lustig *et al* 2007). In CS reconstruction a constrained optimization problem is solved iteratively, in which sparsity is promoted in the transform domain, while maintaining data fidelity by comparing the measured k -space data to the Fourier transform of the reconstructed image. The iterative nature of the reconstruction results in reconstruction time which are considerably longer (up to several hours) than conventional linear reconstruction times.

3. Acquisition strategies for 4D-MRI

As described in section 2, different strategies exist to collect volumetric MRI data. The majority of publications that have appeared of the last few years have focused on developing optimal strategies to generate 4D-MRI data sets. An overview of the recent literature shows that the proposed 4D-MRI methods can be categorized into two distinct groups: multi-slice 2D acquisitions, and 3D acquisitions. Within each group variations in terms of acquisition order, k -space trajectory, or imaging contrast have been described in the literature.

About 40 papers have appeared since 2005 that describe the use of multi-slice 2D imaging to generate 4D-MRI. The use of 3D acquisitions has only been explored more recently. While motion compensation methods by retrospective gating have been investigated for just over a decade, actual 4D-MRI generation for the use of motion characterization has only been described since 2013 for 3D acquisitions. The interest in 3D acquisitions, however, is rising rapidly. In 2017 eight papers discussed 2D acquisitions, while seven papers were published on 3D imaging (see table 1).

3.1. 2D multi-slice methods

The early work on 4D-MRI entirely consists of methods that use 2D multi-slice acquisitions. This is due to the fact that generation of a 4D-MRI data set is easier for 2D acquisitions, because sorting can be performed on the DICOM images (see section 5 for further details). As knowledge on MRI pulse programming or reconstruction is limited in most radiation therapy groups, a DICOM based method provides a practical alternative for the initial development of 4D-MRI.

The published 2D multi-slice approaches have mainly used T2 weighted Turbo spin echo (T_2 -TSE) or balanced steady-state free precession (bSSFP). T_2 -TSE is the main workhorse for delineation of many tumor sites and provides a T_2 weighted image (provided the relaxation time is large enough). bSSFP on the other hand is a very efficient short T_R sequence that provides a T_2/T_1 contrast (Scheffler 1999, Bieri and Scheffler 2013). This sequence is often used in cine MRI to maximize temporal resolution as it provides the highest signal per unit of time by re-using transverse magnetization from one T_R to the next (Nayak *et al* 2005, Miller 2012). Multi-slice 2D acquisitions acquire the data on a slice-by-slice basis. As explained in section 2 the order in which the slices

are acquired can be altered. The exact ordering has an effect on the efficiency of the 4D data collection as well as the possible imaging contrasts as we will see below. Basically the methods can be divided into two groups: prospective and retrospective methods of which the latter can again be subdivided into sequential and cine-mode acquisitions.

3.1.1. Retrospective methods

Sequential imaging is most comparable to a normal (static) image acquisition. In sequential imaging the same volume is acquired multiple times after which the data is retrospectively sorted correlated to the respiratory cycle. The slice ordering in this form of acquisition can either be ascending, descending, or interleaved. All retrospective methods, however, have the disadvantage that the sequence is agnostic of the respiratory waveform during the acquisition. The filling of the respiratory bins during the reordering process is therefore not always ensured (i.e. a certain slice may never be acquired at the right respiratory state). To mitigate the stochastic nature of the acquisition, cine-mode has also been introduced. In cine-mode, the same slice location is acquired multiple times until a complete respiratory cycle is sampled before moving on to the next slice location (Cai *et al* 2011, Liu *et al* 2014). This approach reduces the risk of missing slices in the final 4D-MRI data set. The scan duration per slice location depends on the duration of the respiratory cycle. In the studies that have been published the required scan duration was either determined based on a pre-scan (Cai *et al* 2011) or set conservatively long (Liu *et al* 2014), although in principle it would also be possible to feed back the respiratory signals from e.g. the respiratory bellows during the scan to ensure that the entire respiratory cycle is sampled for each slice location. Steady-state sequences are more suitable for cine-mode imaging, while sequences such as T_2 -TSE are more suitable for sequential imaging due to the requirement for a long T_R .

3.1.2. Prospective methods

In prospective methods the slice ordering is determined on-the-fly based on the respiratory signal (Du *et al* 2015, Glide-Hurst *et al* 2015). Compared to retrospective reordering, prospective methods have improved acquisition efficiency, as they monitor what slices have been acquired and thus avoid re-acquiring slices. Furthermore one can ensure that all slices are collected for each respiratory state. The T_R in prospectively triggered sequences, however, is no longer fixed, but determined by the patient's breathing frequency. To avoid fluctuation in magnetization as a result of changing repetition times care should be taken that complete relaxation has occurred before the same slice location (but for another respiratory state) is acquired again.

Slice orientation is another important consideration. Characteristic of multi-slice 2D acquisition is the high in-plane resolution in combination with a coarse through plane resolution due to the limited slice thickness. Delineations are mostly performed on transversal slices, since most conventional radiation treatment planning systems only accept transverse image, as a result of the fact that they use CT images, which only allow for transversal imaging. For delineation purposes, a transversal acquisition is the most natural orientation to acquire the images in. However, the main direction of (respiratory induced) motion also lies along the feet-head direction, which results in large amount of through plane motion for this orientation. Spins of moving tissue may therefore move from one slice to the next causing image artifacts. In abdominal and thoracic imaging a sagittal orientation is often optimal in order to minimize through plane motion, since left-right motion is generally the smallest and negligible (<2 mm) compared to the slice thickness (Liu *et al* 2014).

As most 2D multi-slice methods use Cartesian readouts, standard image acceleration methods such as partial Fourier and parallel imaging are often employed to reduce scan time. Recently, the use of simultaneous multi-slice (SMS) has also been proposed. In SMS a multi-band RF pulse is used to excite multiple slices, which are simultaneously sampled. As a result the signal from two slices is overlapped, so parallel imaging reconstruction is used to separate the signals that originate from the different slices. To improve the parallel image reconstruction the phase of the multi-band RF pulse is used to shift the relative position of adjacent slices in image space (Breuer *et al* 2005, Stemkens *et al* 2016a). In a paper by Celicanin *et al* (2015), SMS was successfully used to acquire a 2D navigator signal simultaneously with the imaging slice. By changing the distance between two SMS slices the navigator slice could be kept at the same location throughout the experiment, while the imaging slice position was altered to collect the entire volume. The benefit of this approach is that the 2D navigator is collected at the exact same time as the imaging slices. It is, however, questionable whether the additional information of the 2D navigator outweighs the two-fold SMS acceleration factor that is sacrificed to acquire a full 2D navigator for each acquired imaging slice.

A more conventional method to extract respiratory surrogates from imaging data is the use of a separate 1D navigator acquisition, which allows simple extraction of the respiratory motion signal from the 1D projection via cross correlation (Nehrke and Manke 2000). Section 3.4 provides further details on the various surrogate signals that are available to correlate the imaging data to the respiratory waveform.

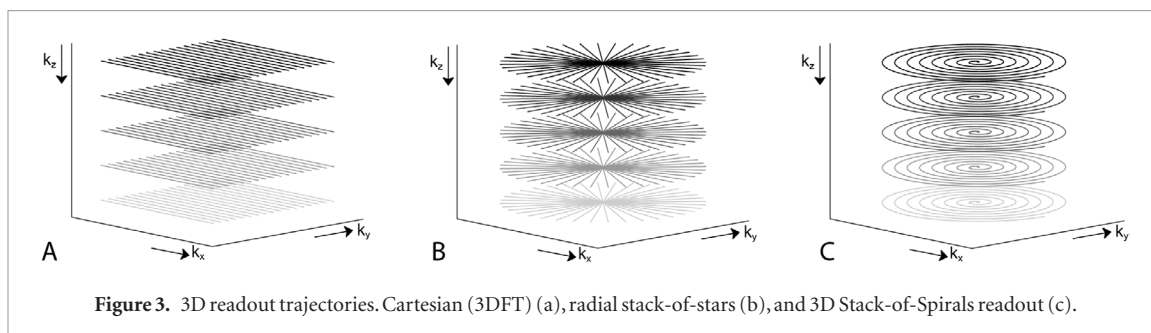


Figure 3. 3D readout trajectories. Cartesian (3DFT) (a), radial stack-of-stars (b), and 3D Stack-of-Spirals readout (c).

3.2. 3D methods

The number of 4D-MRI methods that use 3D readouts is increasing. As a standard 3D readout takes multiple respiratory cycles to collect, the data has to be reordered before image reconstruction (i.e. in k -space). As the development often requires custom pulse sequences and reconstruction algorithms the development of these types of methods are mostly performed by established MR physics research groups. Most papers published so far differ in the readout that is used. The reason for this is two-fold: for one, the readout determines for a large extent the image quality, particularly in the presence of motion. Second, the additional dimension allows for more flexibility in terms of readout trajectory. To date, various 3D readout trajectories have been developed for 4D-MRI that include non-Cartesian, Cartesian, and hybrid readouts (see table 1).

3.2.1. Non-Cartesian readouts

The use of 3D radial, also known as 3D projection imaging or kooshball, has been explored by one group (Yang *et al* 2015b, Deng *et al* 2016, 2017, Park *et al* 2016). The readout consists of a large number of radial projections with different polar and azimuthal angles. A golden means ordering scheme is used (Chan *et al* 2009) to achieve a uniform distribution of sampled lines throughout the acquisition. The benefit of a full 3D readout is the benign point spread function, which allows for very high undersampling factors with benign (incoherent) image artifacts. This property makes radial a very suitable readout strategy for compressed sensing image acceleration. Further, the center of k -space is sampled by each line, which makes the readout very robust. The disadvantages of this readout are that oversampling the center of k -space requires time, which reduces the efficiency of the readout. Also, the reconstruction involves a 3D gridding step, which is computationally expensive. This particularly impacts on the reconstruction speed of iterative reconstructions (i.e. iterative SENSE or CS reconstructions).

3.2.2. Hybrid readouts

One way of mitigating these effects is the use of hybrid radial-Cartesian readouts (Buerger *et al* 2012, Stemkens *et al* 2015, 2016b, 2017b, Rank *et al* 2016b, 2017, Freedman *et al* 2017, Mickevicius and Paulson 2017). These hybrid readouts sample k -space along a radial pattern in two dimensions, while the third is sampled on a Cartesian grid. Two examples that have been described in the more recent 4D-MRI literature are the radial stack-of-stars (SoS) (Stemkens *et al* 2015, 2016b, 2017b, Rank *et al* 2016b, 2017, Freedman *et al* 2017, Mickevicius and Paulson 2017) and the radial phase-encoded readout (Buerger *et al* 2012). Figure 3(b) shows a diagram of the radial SoS. While maintaining the radial sampling pattern in the k_x - k_y plane, the readout uses Cartesian sampling along the k_z -direction. Each shot thus consists of an angulated Cartesian readout in which all the k_z -partitions are acquired. Similar to the 3D radial acquisition subsequent shots are typically rotated by the golden angle (Winkelmann *et al* 2007) to ensure quasi-uniform k -space coverage when the data is undersampled. The benefit of the Cartesian dimension is that the image reconstruction can be parallelized along that dimension and the reconstruction requires 2D rather than 3D gridding. Radial phase encoded MRI takes the opposite approach. Here, Cartesian sampling along readout direction (k_x) is combined with a Golden-order radial sampling scheme in the phase-encoding plane (k_y - k_z) (Buerger *et al* 2013). The benefit of this technique is that typical corrections that are needed for radial acquisition (e.g. eddy-current-related phase errors) are not needed for this type of readout as the readout and phase encode directions are completely separated like in conventional Cartesian imaging.

3.2.3. Cartesian readouts

Cartesian readouts have also been investigated for the use in 4D-MRI. Examples include the rotating Cartesian k -space (ROCK) trajectory proposed by Han *et al* (2017) and the compressed sensing partial subsampling (ESPrESSO) scheme by Küstner *et al* (2017). These methods are similar to the Radial Phase Encode trajectory, but differ by the fact that the PE positions are positioned onto the rasterized (Cartesian) grid. For both methods the undersampling pattern is pseudo-randomly chosen to facilitate compressed sensing reconstruction and reduce coherent motion artifacts.

Table 2. Summary table. List of advantages and disadvantages of 2D and 3D acquisition strategies for generation of 4D-MRI.

	2D multi-slice	3D
SNR		+
Contrast flexibility	+	
Ease of implementation	+	
Geometric corrections		+
Motion averaging		+
Navigation options		+
Image acceleration options		+
Reconstruction speed	+	

Nearly all 3D based methods are self-navigated, which means that the respiratory surrogate signal is obtained directly from the image data, although other approaches such as pencil-beam navigators or respiratory bellows are also possible. Because the entire imaging volume is excited by every RF pulse in 3D acquisitions, the contrast is mostly limited to spoiled gradient echo (SPGR), ultra short echo time (UTE), or bSSFP sequences. 3D T_2 -TSE is possible, but so far has not been used as a native contrast for 3D based 4D-MRI, because of its prolonged T_R to allow for T_1 relaxation and therefore significantly longer acquisition time compared to e.g. SPGR or bSSFP.

3.3. 2D versus 3D methods compared

The implication of using 3D versus 2D imaging for 4D-MRI is substantial (see table 2). First, the time-interval between subsequent excitations of the same tissue is much shorter for 3D acquisitions than for 2D multi-slice imaging. As a result the longitudinal steady-state magnetization that is available for signal formation is lower. On the other hand, the fact that the signal is sampled from the entire volume, rather than a single slice, leads to an intrinsic SNR advantage of $\sqrt{N_{\text{slices}}}$. The fact that the image is Fourier encoded along all three dimensions allows for imaging at high isotropic resolution. The longer readouts, however, make this type of sequence more prone to intra-view motion artifacts if not appropriately dealt with (this ‘problem’ has in fact spurred early work that focused on motion compensation by reordering of the data) (Bailes *et al* 1985, Buerger *et al* 2013).

The short T_R in 3D imaging makes GRE the most natural contrast for 3D acquisitions. This includes spoiled sequences, such as SPGR (or FLASH), that provide pure T_1 contrast as well as steady-state sequences, such as bSSFP, that provide a T_2/T_1 contrast. Depending on whether the 4D-MRI is used for delineation purposes or merely as a motion characterization method (since organ contrast can be limited) this may or may not be a limitation of the current 3D based 4D-MRI methods.

A benefit of 3D readouts versus 2D readouts is the increased flexibility of the additional dimension. This increased flexibility can be exploited to design trajectories that are better suited to acceleration techniques that allow for higher acceleration factors such as 2D GRAPPA and SENSE or compressed sensing. Moreover, the radial readouts used in most 3D based 4D-MRI methods sample the center of k -space with every shot, which ensures that the anatomy represents the average position of all sampled physiological states. A final, but very important implication for radiation therapy applications is the effect of gradient non-linearity. By design the field gradients of any MRI scanner are not perfectly linear over the entire field-of-view. If not taken into account these non-linearities would result in considerable geometric distortions with increasing severity away from isocenter. In principle the non-linearity is carefully mapped by the vendor. This information is subsequently used during reconstruction to correct the geometric distortions via interpolation in image space. The interpolation step, however, requires the acquisition of a contiguous volume and is easier to perform for a 3D acquisition than for multi-slice 2D acquisitions. Hence, some vendors only correct in-plane distortions for 2D acquired images, which severely limits the applicability for radiotherapy. This (uncorrected) slice distortion is referred to as potato chipping and could lead to local displacements of up to four cm when imaging at a distance of 20 cm away from isocenter (Borman *et al* 2018).

3.4. Surrogate signals

Three general approaches have been utilized to guide the reordering of 4D-MRI data: external surrogates, internal surrogates, and self-navigation. A subset of surrogate signals mirrors those of 4D-CT, while others are unique to MRI. Those that mirror 4D-CT include external surrogates such as pneumatic belts (bellows) (Rohlfing *et al* 2004, Tryggstad *et al* 2013, Hu *et al* 2013, Du *et al* 2015, Liu *et al* 2015b), tidal lung volumes (Marx *et al* 2014), and camera-based systems (Remmert *et al* 2007). Challenges with external surrogates include signal saturation, gain resetting, synchronization of start and end times with pulse sequence acquisition, and loss of phase coherence with acquired k -space data (Tryggstad *et al* 2013, Stemkens *et al* 2015). In addition, external surrogate motion may not directly correlate with target or organs at risk (OAR) motion (Feng *et al* 2009, Goldstein *et al* 2010).

Finally, logistics of setup and positioning time, battery life, and MR bore interference can also challenge use of external surrogates for 4D-MRI.

The remaining approaches to guide 4D-MRI reconstruction are unique to MRI. Internal surrogate signals include pencil-beam navigators. Pencil beam navigators are fast 1D MRI acquisitions that utilize 2D radiofrequency pulses to selectively excite a column of spins (Ehman and Felmlee 1989). The navigators can be prescribed with arbitrary orientation over high contrast interfaces of moving structures closest to the target or structure of interest. The most common navigator prescription is the lung-liver interface (Stemkens *et al* 2015). However, navigators can also be placed at the kidney/perirenal fat interface. During acquisition, two sequences are executed: (i) the parent sequence consisting of pencil-beam navigator sampling, (ii) the child sequence consisting of the desired contrast weighting. Although the pencil-beam navigator signal may correlate with target or OAR motion, the parent/child relationship of the acquisition decreases scanning efficiency when pencil beam navigators are used (Buerger *et al* 2013). Furthermore, disruption of the imaging steady-state can occur, which can complicate pencil-beam navigator use with coherent and incoherent steady state free precession pulse sequences for 4D-MRI (Scheffler and Lehnhardt 2003). Lastly, for 3D acquisition the pencil-beam navigator can saturate part of the imaging volume, if placed inside the desired imaging volume.

Self-navigation (also often referred to as self-gating or self-guidance) is a process by which the acquired MRI data itself can be used to detect motion and/or correct for motion artifacts during image reconstruction. In terms of 4D-MRI, self-navigation is used to reorder the acquired data during 4D-MR reconstruction. Self-navigation has been performed in both the image and frequency domains. Image domain methods have included 2D image navigators (Von Siebenthal *et al* 2007, Celicanin *et al* 2015) and changes in body surface area (Cai *et al* 2011, Liu *et al* 2014, Yang *et al* 2014). For 2D image navigators, 2D images are acquired over complete respiratory cycles in either a cine (Würslin *et al* 2013, Bernatowicz *et al* 2016) or sequential (Celicanin *et al* 2015) acquisition strategy. Image registration is then used to reorder the acquired images into respiratory bins. This method can be enhanced using SMS acquisitions (Celicanin *et al* 2015). Image registration of the 2D image navigator is then used to reorder the 2D images into different respiratory bins. Cross-correlation of 1D projections (Buerger *et al* 2013, Deng *et al* 2016, Han *et al* 2017, Mickevicius and Paulson 2017), or changes in centroid positions of 1D projections (Küstner *et al* 2017), obtained from Fourier transform along the k_z direction in 3D acquisitions, is an additional image-domain self-navigation approach. Finally, self-navigation can also be based on the thermal noise variance of the receive coils during acquisition (Andreychenko *et al* 2017). Frequency domain self-navigation has also been performed to reshuffle 4D-MR data (Hui *et al* 2016, Rank *et al* 2017). One frequency domain approach is based on variations in the amplitude of the k -space center (i.e. DC signal) of 3D acquisitions (Rank *et al* 2017). Another method is based on the Fourier shift theorem, in which phase ramps in the frequency domain corresponds to shifts in the image domain (Hui *et al* 2016). Challenges with self-navigators include phase instability, eddy currents, and partial saturation bands (in the context of 2D image-based self-navigators). Advantages include increased efficiency and direct synchronization with the imaging data.

4. Generating a respiratory-correlated data set

Once MR data is acquired and a respiratory surrogate signal is extracted with good temporal correlation with the MR data, a 4D-MRI can be generated. Depending on the MR acquisition (i.e. the read-out), data are sorted in image- or k -space, using the respiratory information from the surrogate signal. If necessary, additional processing steps are done after sorting the data, primarily for k -space based methods.

4.1. Binning

Sorting of the data can be done in a number of ways, similar to sorting 4D-CT data. These data can be k -space data or images. In general, there are two ways of sorting the data; based on the amplitude of the respiration (*amplitude binning*), or based on the phase of the respiration (*phase binning*). In amplitude binning, data within a certain range of respiratory amplitudes is assigned to one of n equally spaced amplitude bins, based on the full respiratory signal (see figure 4(a)). For phase binning, each breathing cycle is divided into n equal time bins, in which all data is sorted (see figure 4(c)). The number of bins n can be chosen freely, but is generally between four and ten, since 4D-CT also generates ten bins. Overall, less bins requires less data, but introduces more intra-bin variability. Often the peaks and troughs of the respiratory signal are extracted, representing end-exhale and—inhale point, to determine the respiratory phase. The majority of the published 4D-MRI (and 4D-CT) methods used phase-based sorting, since phase-based sorting intrinsically holds probabilistic information that is useful for radiotherapy planning, i.e. the time spent in each phase is equal for phase binning. Therefore, these data can readily be used to generate an ITV margin, which is the overlapping tumor position over all respiratory phases, or a mid-pos volume, which is the time-averaged position. Additionally, amplitude binning may require much longer acquisition times due to breathing variations, such as baseline drifts.

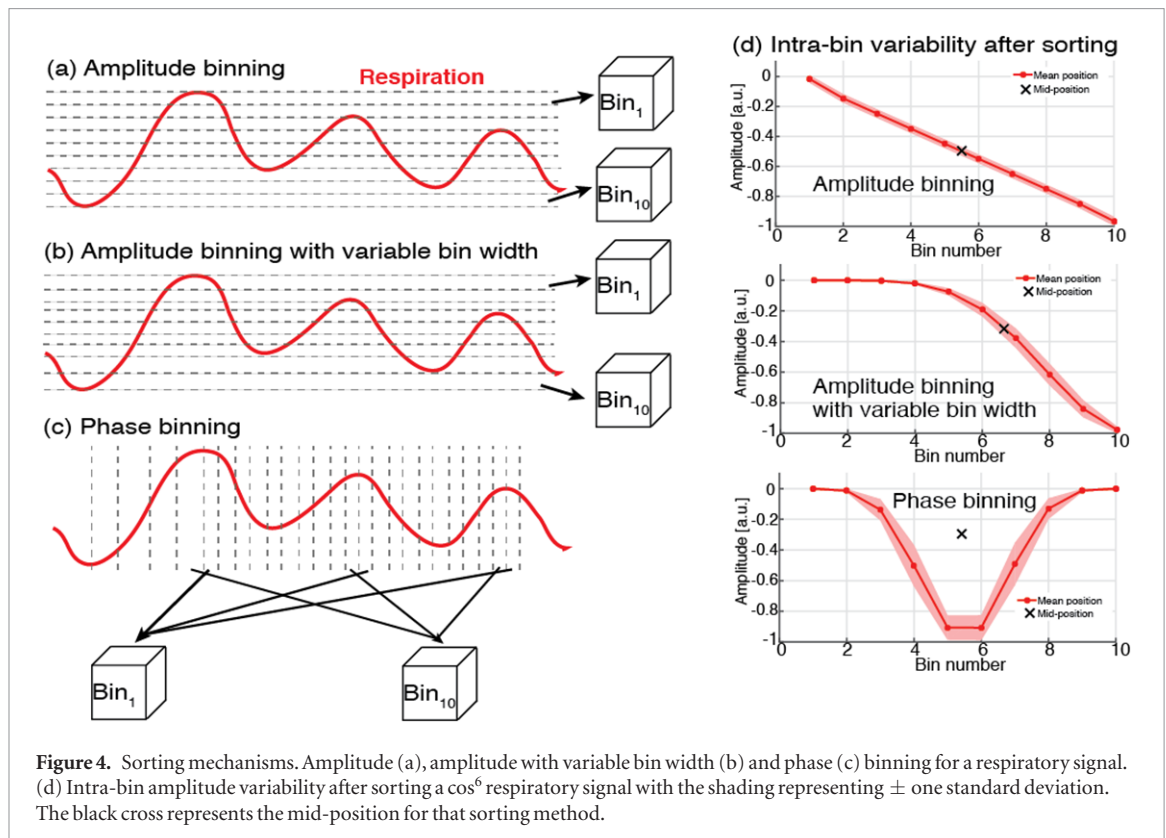


Figure 4. Sorting mechanisms. Amplitude (a), amplitude with variable bin width (b) and phase (c) binning for a respiratory signal. (d) Intra-bin amplitude variability after sorting a \cos^6 respiratory signal with the shading representing \pm one standard deviation. The black cross represents the mid-position for that sorting method.

Exceptions are prospectively gated methods, which generally employ amplitude binning. These prospective methods acquire data (in general 2D images) at a given amplitude, based on surrogate signals, such as respiratory bellows (Rohlfing *et al* 2004, Hu *et al* 2013, Du *et al* 2015, Glide-Hurst *et al* 2015, To *et al* 2016, Li *et al* 2017), or 1D MR navigators (Tokuda *et al* 2008, Li *et al* 2017). While the probabilistic information is also available for amplitude binning, since the amount of data for each bin is known after sorting, it can only be extracted by calculating the probability density function (PDF) and, if necessary, convolving the data with this PDF (Engelsman *et al* 2005). Alternatively, amplitude binning with variable bin width can be used, where the width of each amplitude bin varies such that the amount of data in each bin is equal (see figure 4(b)). Consequently, probabilistic information is included using such a sorting approach.

For 4D-CT it was concluded that amplitude sorting can significantly improve image quality and reduce artifacts (Fitzpatrick *et al* 2005, Rietzel *et al* 2005, Wink *et al* 2006, Abdelnour *et al* 2007, Lu *et al* 2006). Typical 4D-CT artifacts, such as blurring, duplicate structures, overlapping slices and incomplete structures (Yamamoto *et al* 2008) were significantly reduced when amplitude sorting was used. However, it was also reported that amplitude binning could result in insufficient data at specific couch positions when no data is acquired at certain amplitudes (Abdelnour *et al* 2007, Yamamoto *et al* 2008). Moreover, amplitude binning generally does not discriminate between exhale and inhale. Thus, hysteresis, the phenomena that respiration is different when inhaling compared to exhaling, cannot be captured. While this may be no problem when determining the maximum respiratory-induced motion, both the mid-position volume and ITV margin are different when including or excluding hysteresis effects. Nevertheless, hysteresis can also be characterized through amplitude binning, by dividing the respiratory cycle into ex- and inhale and sorting identical amplitudes into either ex- or inhale amplitude bins (Li *et al* 2017, Hu *et al* 2013).

The image quality and artifact level of the reconstructed 4D-MRI partly depend on the sorting method. The sorting method, number of bins, and variability of the respiration determine the variations that are present within each bin, i.e. the intra-bin variability. For both k -space and image-based methods, larger intra-bin variability results in increased artifacts and decreased image quality. Since different amplitude data are sorted into the same bin, the mean position of that bin is an average of all these amplitudes. This typically leads to a small underestimation of the motion when compared to 2D cine MR imaging.

A simulation where a \cos^6 respiratory signal (which is commonly used to simulate respiratory motion (Lujan *et al* 1999)) is sorted into ten bins using different methods shows that the mean bin position and the intra-bin amplitude variability (i.e. the variations in amplitude that are sorted into a single bin), shown by the dots and transparent area, respectively, vary between the different methods (see figure 4(d)). Consequently, the mid-position will be different, as well as the image quality after sorting.

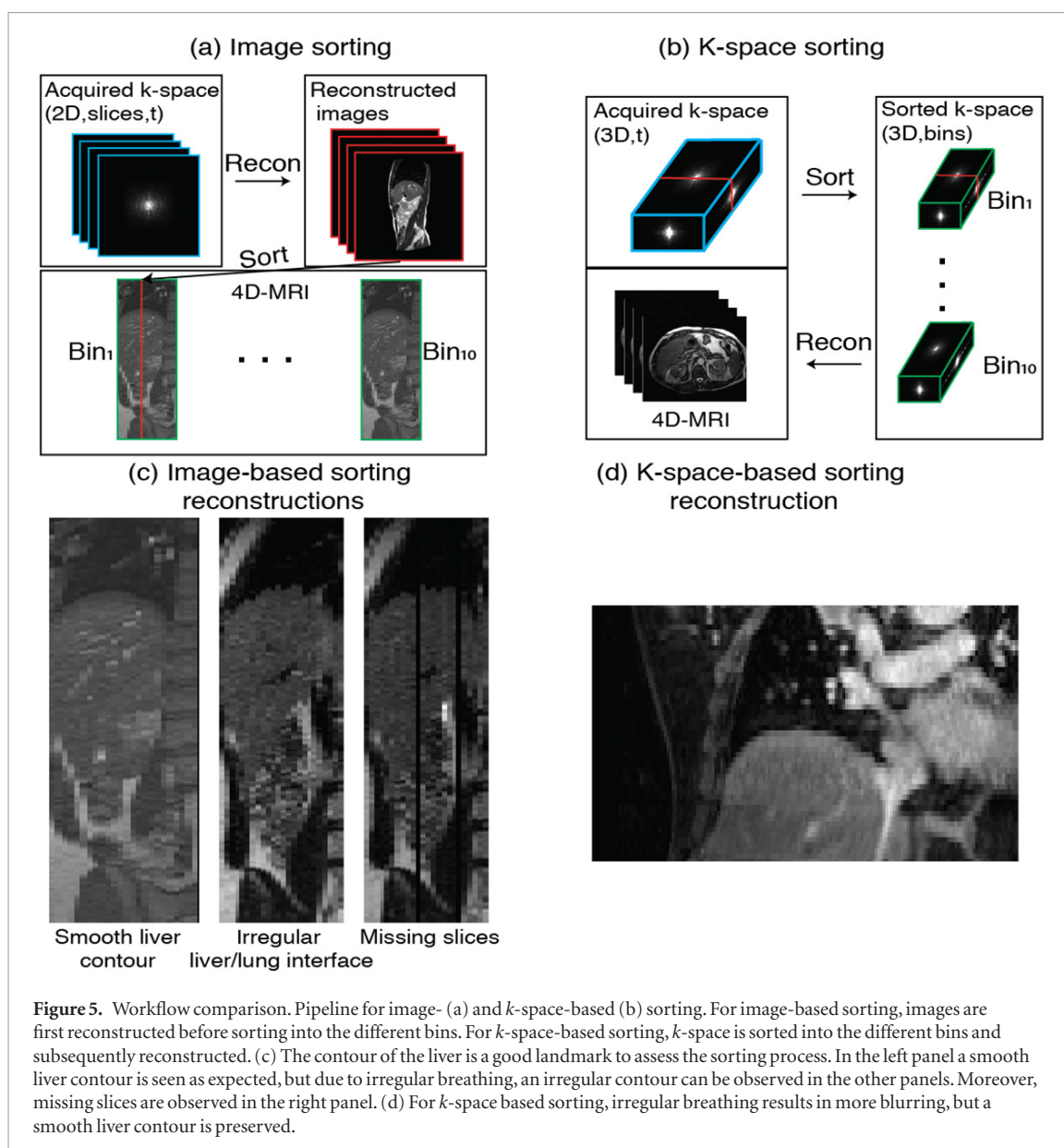


Figure 5. Workflow comparison. Pipeline for image- (a) and k -space-based (b) sorting. For image-based sorting, images are first reconstructed before sorting into the different bins. For k -space-based sorting, k -space is sorted into the different bins and subsequently reconstructed. (c) The contour of the liver is a good landmark to assess the sorting process. In the left panel a smooth liver contour is seen as expected, but due to irregular breathing, an irregular contour can be observed in the other panels. Moreover, missing slices are observed in the right panel. (d) For k -space based sorting, irregular breathing results in more blurring, but a smooth liver contour is preserved.

Overall, different flavors of binning exist for 4D-MRI. While amplitude binning may give smaller intra-bin amplitude variations, phase binning inherently contains probabilistic information that may be useful in radiotherapy treatment planning.

4.2. Image- versus k -space based sorting

In general, 2D acquired data is first reconstructed into images before sorting in the image domain. 3D acquisitions, on the other hand, are sorted in k -space and subsequently reconstructed. Consequently, image-based sorting has been used more in earlier publications, while k -space sorting gained popularity in recent years. For prospective methods, image data is already sorted into the different bins immediately after acquisition, so no additional sorting has to be performed.

4.2.1. Image-based sorting

In image-based sorting, 2D images (or 3D volumes) are first reconstructed (on the scanner) and subsequently sorted into the respiratory bins, based on the surrogate signal using amplitude or phase binning (see figure 5(a)). The liver-lung interface in the slice direction is often used to determine the accurateness of sorting, since a smooth liver top (i.e. diaphragm shape) is expected (see figure 5(c), left panel, for coronal view of sagittally acquired images). Irregular breathing may give rise to an irregular liver contour (see figure 5(c), middle panel), so-called ‘stitching artifacts’. After sorting it may happen that at certain slice locations and bins, multiple image slices are present (oversampled). Either the first or last image can be used, or the image with the highest similarity with surrounding slices (Tryggstad *et al* 2013). Conversely, it can also happen that no image is assigned at a certain location and bin, leading to black bands in the reconstructed volumes (see figure 5(c), right panel). This can

happen when this slice location was insufficiently sampled, or, for amplitude binning, this respiratory amplitude was not encountered during sampling. The missing image can be extracted by interpolating from different slice locations or different phases, or by taking the slice from an adjacent phase (Cai *et al* 2011, Cai *et al* 2015, Liu *et al* 2015a, 2015b, Yang *et al* 2014, 2015). A longer acquisition minimizes the risk of missing slices, but increases overall scan time. If 2D data is acquired in cine-mode, at least one respiratory cycle (5–10 s) has to be acquired per slice location to sample sufficient data.

4.2.2. *K*-space sorting

In *k*-space sorting, parts of *k*-space are sorted into different phase volumes and subsequently reconstructed to image space (see figure 5(b)). This can be a single *k*-space line, *k*-space segments or an entire *k*-space, given that the respiratory amplitude/phase for that part of *k*-space is known. Most *k*-space-based sorting methods use 3D non-Cartesian MR sampling (Buerger *et al* 2012, Stemkens *et al* 2015, Yue *et al* 2015a, 2015b, Deng *et al* 2016, 2017, Rank *et al* 2016a, 2017, Freedman *et al* 2017, Mickevicius and Paulson 2017), while some used Cartesian sampling in 2D (Liu *et al* 2015b) or 3D (Stemkens *et al* 2015, Küstner *et al* 2017). An advantage of *k*-space sorting, and non-Cartesian sampling in particular, is that missing data does not lead to black lines in the reconstructed volumes, but to an increase of undersampling artifacts, which manifest as aliasing in Cartesian and streaking in radial sampling. Moreover, if multiple identical *k*-space segments are sorted into a certain bin, complex averaging can be used to increase SNR. After sorting, data is transformed to image space using an inverse FFT. For non-Cartesian sampling this is preceded by a gridding step which convolves data onto a Cartesian grid (Fessler *et al* 2003). Since all data within a bin contribute equally, the reconstructed volumes represent the average position of the anatomy during data acquisition of the *k*-space segments that are within that bin (see figure 5(d)).

4.2.3. Comparison

K-space- and image-based sorting both have advantages and disadvantages. Advantages of *k*-space sorting are that undersampling is less problematic, the temporal resolution of a segment that is sorted can be much higher (e.g. a single *k*-space line), and it can be used with 3D acquisitions. Additionally, for non-Cartesian *k*-space sorting methods, irregular breathing leads to increased blurring in the reconstructed images, while for image-based sorting methods this generally results in an irregular liver contour (see figures 5(c) and (d)). However, *k*-space-based methods are generally more difficult to implement and reconstruction may take longer, as the entire reconstruction is usually performed offline. So far no prospective methods have been proposed with *k*-space sorting. Image-based methods are generally based on 2D acquisitions that provide more freedom in choice of contrast (see section 3).

4.3. Compressed sensing and its effect on motion smoothness

While for image-based methods no additional steps have to be taken after sorting (except for filling in missing slices), 3D *k*-space-based methods often employ additional reconstruction steps. In recent years, a trend towards shorter acquisitions is seen to reduce acquisition time. Consequently, undersampling artifacts increase in the reconstructed 4D-MRI. To minimize these undersampling artifacts iterative reconstructions were proposed for non-Cartesian 3D acquisitions. Examples are non-Cartesian iterative SENSE (Pruessmann *et al* 2001) in Buerger *et al* (2012), or compressed sensing (CS) (Lustig *et al* 2007) with different regularization terms in Freedman *et al* (2017), Mickevicius and Paulson (2017), Rank *et al* (2017) and Stemkens *et al* (2017b). CS reconstructions exploit image sparsity in one or more domains (spatial or temporal). For 4D-MRI, total variation (TV) sparsity in the temporal domain were suggested (Mickevicius and Paulson 2017) as well as the motion-correction high-dimensional TV in both spatial and temporal domain (Rank *et al* 2017). Increasing the regularization using these sparsifying constraints results in smoother images with reduces artifacts, but may also underestimate the motion in the resulting 4D-MRI (Mickevicius and Paulson 2017). Essentially, the motion within the 4D-MRI is smoothed as a result of the CS reconstruction. Note that such iterative reconstructions are computationally intensive and take anywhere between a few minutes (Mickevicius and Paulson 2017) to several hours (Rank *et al* 2017). Although CS is a valuable technique to minimize artifacts for severely accelerated 4D-MRI acquisitions, care should be taken when using CS and any motion underestimations should be accessed and quantified. Lastly, the same amount of data should be present in each bin, so these methods use amplitude binning with variable bin width, or phase-based binning.

4.4. Reconstruction challenges

Most 4D-MRI techniques described in the literature perform the reconstruction (i.e. surrogate extraction, sorting and image reconstruction if necessary) offline on a separate PC. Exceptions are prospective methods that have to keep track of the acquired data on the scanner and are therefore generally reconstructed on the scanner. In order to use 4D-MRI in a clinical setting, a robust reconstruction is required that generates the 4D-MRI automatically and sends the 4D-MRI to a picture archiving and communication system (PACS) or

other DICOM server. This way the 4D-MRI is included in the clinical process and is accessible for viewing to clinicians. Ideally, an online implementation is employed where the 4D-MRI is immediately reconstructed on the scanner, similar to prospective methods. However, this is often difficult, since non-standard reconstruction steps are used. This is something that needs to be picked up by the vendors. Several vendors are already introducing CS type of reconstructions on the market, so the step towards 4D-MRI implementations could be relatively small. Alternatively, large departments may choose to set up their own reconstruction pipeline where acquired data is (automatically) reconstructed on an offline server and pushed to PACS. An advantage of such an infrastructure is that computationally extensive reconstructions, such as CS, can run overnight. Having a robust and automatic 4D-MRI reconstruction pipeline is essential for clinical introduction and larger patient studies.

5. Current and potential clinical application of 4D-MRI

4D-MRI can be integrated into the clinical radiotherapy workflow at different steps. During MR simulation, 4D-MRI can be used to construct high-quality, static, reference images for treatment plan generation, including mid-ventilation (van de Lindt *et al* 2016), mid-position (Wolthaus *et al* 2008b, Kontaxis *et al* 2017), or alternate respiratory phase images. Leveraging its soft tissue contrast benefits, target and organ at risk (OAR) delineation accuracy may improve with 4D-MRI compared to 4D-CT (Hu *et al* 2013, Yang *et al* 2015c). Target and OAR motion models for margin assessment and construction of motion structures (e.g. internal target volumes or planning risk volumes) can be determined from 4D-MRI that may not suffer from motion underestimation and stitching artifacts as in 4D-CT (Yang *et al* 2015c). 4D-MRI can also be used to establish 4D deformation vector fields (DVF), which could be used for example, as vehicles to align additional MR image contrasts, obtained during MR simulation, to specific respiratory phases or motion states of reference images (Freedman *et al* 2017). This may be particularly important, in that it enables MR images to be acquired at a particular respiratory phase more suitable for acquisition (e.g. inhalation breath hold) and then warped to a particular respiratory phase more suitable for treatment (e.g. end-expiration). The motion models, coupled with review of the 4D-MR surrogate or self-navigator signal, can be used to determine whether a particular patient may be a good candidate for respiratory gated radiotherapy delivery and, if so, selection of gating windows.

4D-MRI can also be integrated for pre-beam, beam-on, and post-beam phases of in-room, hybrid MR-guided radiotherapy devices (Fallone 2014, Keall *et al* 2014, Mutic and Dempsey 2014, Lagendijk *et al* 2016). During the pre-beam phase of treatment, 4D-MRI can be used to construct high-quality reference images capturing the anatomy and motion of the day. This information could be used in clinical decision support for evaluating whether plan adaptation is required prior to delivery. Moreover, 4D-MRI can be used to generate synthetic (4D-)CT images for planning in conventional treatment planning or for daily plan optimization. In addition, motion models derived from pre-beam 4D-MRI can be used to determine the optimal alignment of real-time cine imaging planes (i.e. to capture the largest displacements) to monitor target and/or OAR motion during the beam-on phase of treatment. Real-time cine MR images acquired during beam-on can be used to drive the pre-beam motion models to construct synthetic 3D image volumes at the temporal resolution of these real-time cine images (Stemkens *et al* 2016b, Harris *et al* 2018). The synthetic 3D volumes can be used, in combination with the synthetic (4D-)CT data, in the post-beam phase to reconstruct the dose delivered during the treatment fraction, providing a mechanism to perform ‘truth-in-delivery’ analysis (Stemkens *et al* 2017b). The reconstructed dose could then be accumulated and eventually fed back into the adaptive planning process for the next treatment fraction (Kontaxis *et al* 2015). The real-time cine MR imaging should be as fast as possible and cover at least the main direction of motion of the target. Using orthogonal cine-MRI, 3D motion of the target can be determined. Since the goal of this real-time imaging is to accurately pinpoint the target (and/or OAR) position, the image quality should be sufficient for the registration or tracking algorithm to determine the target position accurately. For the optical flow algorithm, it has been reported in literature that it performs accurately even when SNR is low (Roujol *et al* 2011), voxel size is large ($5 \times 5 \times 5 \text{ mm}^3$ for 3D imaging) (Glitzner *et al* 2015), and radial undersampling streaking artifacts are present (Stemkens *et al* 2013).

6. Validation of 4D-MRI

A multitude of approaches have been employed to validate 4D-MRI. Motion surrogates have been validated against respiratory bellows waveforms (Tryggstad *et al* 2013, Stemkens *et al* 2015, Hui *et al* 2016, Andreychenko *et al* 2017). Motion amplitudes have been validated by digital (Cai *et al* 2011, Liu *et al* 2016) and physical phantoms (Remmert *et al* 2007, Tokuda *et al* 2008, Cai *et al* 2011, Celicanin *et al* 2015, Yue *et al* 2015b, Deng *et al* 2016, Han *et al* 2017), comparison against cine MRI (Yang *et al* 2014, Deng *et al* 2016, Han *et al* 2017), and comparison against 4D-CT (Yang *et al* 2014, 2015c, Yue *et al* 2015b, Bernatowicz *et al* 2016). However, each of these approaches suffers from confounding effects that obscures direct validation. Respiratory bellows signals may demonstrate loss of phase coherence with acquired data (Tryggstad *et al* 2013). Digital and physical

phantoms may not accurately depict the complex motions observed *in vivo*. In addition, target contrast in dynamic motion phantoms is often markedly different, which almost certainly impacts image registration (Yue *et al* 2015b). Furthermore, due to contrast differences, visualization of dynamic phantom targets may require alternative pulse sequence parameters compared to those used *in vivo*.

Validation with cine MRI is typically performed by comparing sequential, cine MRI and 4D-MRI acquisitions obtained in the same scanning session. However, irregular breathing, baseline shifts, and organ filling between acquisitions may challenge validation. In addition, cine MRI is often acquired with a small number of 2D imaging slices, which may not fully characterize 3D motion and may underestimate displacements in cases with substantial through-plane motion. With improvements in SMS imaging, in which multiple 2D cine imaging slices can be acquired concurrently, these challenges may be reduced but still not eliminated.

Similar to cine MRI, separate 4D-CT and 4D-MRI acquisitions can challenge motion comparisons. However, unlike cine MRI, the patient must be completely repositioned between 4D-CT and 4D-MRI acquisitions, which can exacerbate dissimilarities. In addition, the low soft-tissue contrast of 4D-CT, coupled with its reduced contrast-to-noise ratio (Wolthaus *et al* 2008b), can complicate delineation of solid tumors used for motion comparison (Hu *et al* 2013, Tai *et al* 2013, Yang *et al* 2015c). Finally, it has been well established that 4D-CT may underestimate motion displacements, which can be further affected by stitching artifacts during 4D-CT reconstruction (Watkins *et al* 2010). Despite the abovementioned validation challenges, 4D-MRI motion amplitude agreements within 2 mm or less have been reported (Yue *et al* 2015b, Deng *et al* 2016, Mickevicius and Paulson 2017, Han *et al* 2017).

7. Future of 4D-MRI

The term 4D-MRI is an ambiguous term. A quick literature search reveals that the fourth dimension can either refer to time or a physiological dimension (e.g. the cardiac or respiratory cycle). Major applications that are dubbed 4D-MRI are: 4D cardiovascular imaging, 4D MR Angiography, and 4D Flow imaging. In nearly all cases the fourth dimension refers to the physiological dimension (i.e. the respiratory or cardiac cycle) and not time since the speed of the MRI acquisition is generally too slow to resolve these processes in time. Similarly, in 4D-MRI for radiation oncology, the topic of this review, '4D' refers to *respiratory-correlated* MRI, rather than *time-resolved* MRI. It is important to make a clear distinction between *respiratory-correlated* and *time-resolved* MRI, as the terminology is likely to shift at a certain point when time-resolved MRI does become feasible. The last two decades have mainly focused on hardware development and image acquisition, which together have enabled a 20-fold image acceleration (Sodickson and Manning 1997, Pruessmann *et al* 1999, 2001, Griswold *et al* 2002, Breuer *et al* 2006, Blaimer *et al* 2006). Currently we see strong advances in image reconstruction (Lustig *et al* 2007, Hammernik *et al* 2018). It is anticipated that this will enable another 5- to 10-fold acceleration. Eventually, *true* 4D MRI, in which the physiological motions are actually resolved in time manner, will become possible.

7.1. Current technological developments

Current developments focus on enhancing the impact and applicability of 4D-MRI. One technological development, currently explored by several groups, is the use of motion models to fill the gap between *pre-treatment* 4D-MRI and fast 2D imaging *during* treatment delivery. In each of the currently proposed methods, the volumetric information obtained by the respiratory correlated 4D-MRI is projected onto the fast incoming 2D imaging slices in order to create synthetic time-resolved 4D imaging (Harris *et al* 2016, Stemkens *et al* 2016b, Paganelli *et al* 2018). The generated volumetric time-series can then be used for dose accumulation mapping (Stemkens *et al* 2017b).

Another recent development is the extension of 4D-MRI to a fifth dimension. Here the fifth dimension can either be another physiological dimension (e.g. the cardiac cycle), or a functional contrast dimension (e.g. the dynamic signal enhancement curve in Dynamic Contrast Enhanced Imaging). Although intended as a motion compensation methods for radiological exams (Chandarana *et al* 2015, Feng *et al* 2016), these methods could serve radiation oncology as well as a dual purpose sequence, in which functional imaging is combined with motion characterization (Stemkens *et al* 2017a).

Finally, we are likely to see the extension to multi-echo 4D-MRI in order to generate 4D synthetic CT data. Combining 4D imaging with synthetic CT generation will enhance the accuracy of current dose accumulation methods on the MR-Linac, which currently still use a bulk density assignment.

7.2. Limitations for clinical Implementation

The major reason that 4D-MRI is still only used in research setting is the fact that none of the MRI vendors currently offer 4D-MRI as a product, although some vendors are currently testing prototype implementations. Siemens, for example, is exploring a work-in-progress (WIP) 4D radial stack-of-stars acquisition, whereas Philips is investigating the use of multi-slice 2D MRI. Before these methods can be clinically introduced, however,

a few refinements are needed. For methods that employ 3D readouts it would be desirable to have the flexibility to acquire T2w contrast as well as the current T1-weighted gradient echo contrast. Recent work has shown that hybrid acquisitions that provide both T1w and T2w contrast are indeed possible (Benkert *et al* 2018). For the multi-slice 2D acquisitions gradient non-linearity correction in all three dimensions (including through-plane) is a must for radiotherapy purposes. Further, a prospective stopping criterion, which automatically stops the acquisition as soon as the data sufficiency conditions are met, would help in reducing the overall scan time. For that same reason the ability to generate synthetic CT data, thereby bypassing the need for a separate acquisition, would allow the implementation of 4D-MRI into an MRI-only workflow. It has to be noted, however, that for anatomical sites, such as lung (for which PET imaging is a standard pre-treatment imaging modality) the CT obtained during the PET-CT acquisition will likely remain leading for quite some time.

7.3. Adaptive imaging

Respiratory motion is not the only type of motion that plays an important role in radiotherapy. Other types of motion are bulk motion, drifting, organ filling and bowel peristalsis in the abdomen, and cardiac pulsation in thoracic imaging. With recent data showing poorer survival due to increased heart dose (McWilliam *et al* 2017) it is more than likely that the increased imaging speed will be put to use to critically sample the heart pulsation as well in order to accurately monitor the dose to the heart. On the other hand, the slower types of motion, like bulk motion drift and peristalsis could already be tracked by sequences, such as the golden angle radial readout, which allow sliding window image reconstructions at various temporal resolutions (Winkelmann *et al* 2007). It is to be expected that these types of acquisitions, originally developed for radiological purposes, will be adapted to the requirements within radiotherapy (Bruijnen *et al* 2018).

7.4. Requirements to go real-time

The ongoing developments in image acceleration cultivate the desire of real-time volumetric imaging. Clinical acquisition times of fast 3D imaging are in the order of 20 s (a single breath hold imaging) with a resolution of $2 \times 2 \times 2 \text{ mm}^3$. It is possible to further increase the imaging speed by reducing the resolution. Glitzner *et al* (2015) have demonstrated that a resolution of $5 \times 5 \times 5 \text{ mm}^3$ is feasible for image registration and tumor motion tracking. On the other hand CS has shown to allow image reconstructions of highly undersampled data enabling image acquisition with a resolution of $1.1 \times 1.1 \times 2 \text{ mm}^3$ at a 3.2 s time interval (Kim *et al* 2016). Although highly successful in offline, retrospective, image applications, the long image reconstruction times (often in the order of minutes to hours) prohibit its online, real-time, use. Recently, however, deep learning (DL) image reconstruction has been introduced (Hyun *et al* 2017, Hammernik *et al* 2018, Han *et al* 2018, Qin *et al* 2017). DL has the potential to bypass the reconstruction time problem by shifting the computational burden to a pre-learning phase, while being extremely fast during the actual acquisition. Although some papers have been published on this, the application of real-time imaging has not yet been explored.

8. Conclusions

This review focused on the nuts and bolts of implementing and using respiratory-correlated 4D-MRI for radiotherapy purposes. Because of its high versatility we will most likely see more 4D-MRI implementations in the near future. It is expected that *k*-space-based 3D methods will be used more often moving forward, since their main disadvantages (i.e. long computation times and difficult reconstructions) are more likely to be solved in the foreseen future than the artifacts inherent to image-based multi-slice methods, such as potato chipping and missing data. Collaboration with MRI vendors who choose to implement solid 4D-MRI methods will eventually lead to true time-resolved 4D-MRI.

Acknowledgments

This work is part of the research programme HTSM with project number 15354, which is (partly) funded by the Netherlands Organisation for Scientific Research (NWO).

ORCID iDs

B Stemkens  <https://orcid.org/0000-0003-0488-8070>

References

- Abdelnour A F *et al* 2007 Phase and amplitude binning for 4D-CT imaging *Phys. Med. Biol.* **52** 3515–29
- Andreychenko A, Raaijmakers A J E, Sbrizzi A, Crijns S P M, Lagendijk J J W, Luijten P R and van den Berg C A T 2017 Thermal noise variance of a receive radiofrequency coil as a respiratory motion sensor *Magn. Reson. Med.* **77** 221–8

- Arnold P, Preiswerk F, Fasel B, Salomir R, Scheffler K and Cattin P C 2011 3D organ motion prediction for MR-guided high intensity focused ultrasound *Med. Image Comput. Assist. Interv.* **14** 623–30
- Bailes D R, Gilderdale D J, Bydder G M, Collins A G and Firmin D N 1985 Respiratory ordered phase encoding (ROPE): a method for reducing respiratory motion artefacts in MR imaging *J. Comput. Assist. Tomogr.* **9** 835–8
- Benkert T, Mugler J P, Rigue D S, Sodickson D K, Chandarana H and Block K T 2018 Hybrid T2- and T1-weighted radial acquisition for free-breathing abdominal examination *Magn. Reson. Med.* **80** 1935–8
- Bernatowicz K, Peroni M, Perrin R, Weber D C and Lomax A 2016 Four-dimensional dose reconstruction for scanned proton therapy using liver 4DCT-MRI *Int. J. Radiat. Oncol. Biol. Phys.* **95** 216–23
- Bernstein M A, King K F and Zhou X J 2004 *Handbook of MRI pulse Sequences* (New York: Academic)
- Bieri O and Scheffler K 2013 Fundamentals of balanced steady state free precession MRI *J. Magn. Reson. Imaging* **38** 2–11
- Blackall J M, Ahmad S, Miquel M E, McClelland J R, Landau D B and Hawkes D J 2006 MRI-based measurements of respiratory motion variability and assessment of imaging strategies for radiotherapy planning *Phys. Med. Biol.* **51** 4147–69
- Blaimer M, Breuer F A, Mueller M, Seiberlich N, Ebel D, Heidemann R M, Griswold M A and Jakob P M 2006 2D-GRAPPA-operator for faster 3D parallel MRI *Magn. Reson. Med.* **56** 1359–64
- Borman P, Tijssen R H N, Bos C, Moonen C T W, Raaymakers B W and Glitzner M 2018 How the sampling strategy of 2D MRI affects imaging latencies in real-time MR-guided radiotherapy *6th MR in RT Symp. MR in RT* pp 1–2
- Boye D, Lomax T and Knopf A 2013 Mapping motion from 4D-MRI to 3D-CT for use in 4D dose calculations: a technical feasibility study *Med. Phys.* **40** 061702
- Breuer F A, Blaimer M, Heidemann R M, Mueller M F, Griswold M A and Jakob P M 2005 Controlled aliasing in parallel imaging results in higher acceleration (CAIPIRINHA) for multi-slice imaging *Magn. Reson. Med.* **53** 684–91
- Breuer F A, Blaimer M, Mueller M F, Seiberlich N, Heidemann R M, Griswold M A and Jakob P M 2006 Controlled aliasing in volumetric parallel imaging (2D CAIPIRINHA) *Magn. Reson. Med.* **55** 549–56
- Breuer K et al 2018 Stable and efficient retrospective 4D-MRI using non-uniformly distributed quasi-random numbers *Phys. Med. Biol.* **63** 075002
- Bruijnen T, Stemkens B, Lagendijk J J W, van den Berg C A T and Tijssen R H N 2018 Multi-resolution radial MRI to Reduce IDLE time in pre-beam imaging on an MR-Linac (MR-RIDDLE) *6th MR in RT Symp.*
- Buerger C, Clough R E, King A P, Schaeffter T and Prieto C 2012 Nonrigid motion modeling of the liver from 3-D undersampled self-gated golden-radial phase encoded MRI *IEEE Trans. Med. Imaging* **31** 805–15
- Buerger C, Prieto C and Schaeffter T 2013 Highly efficient 3D motion-compensated abdomen MRI from undersampled golden-RPE acquisitions *Magn. Reson. Mater. Phys. Biol. Med.* **26** 419–29
- Cai J, Chang Z, Wang Z, Segars W P and Yin F-F 2011 Four-dimensional magnetic resonance imaging (4D-MRI) using image-based respiratory surrogate: a feasibility study *Med. Phys.* **38** 6384–94
- Cai J, Liu Y and Yin F 2015 Extracting breathing signal using fourier transform from cine magnetic resonance imaging *Cancer Trasl. Med.* **1** 16–20
- Celicanin Z, Auboiroux V, Bieri O, Petrusca L, Santini F, Viallon M, Scheffler K and Salomir R 2013 Real-time method for motion-compensated MR thermometry and MRgHIFU treatment in abdominal organs *Magn. Reson. Med.* **1095** 1087–95
- Celicanin Z, Bieri O, Preiswerk F, Cattin P, Scheffler K and Santini F 2015 Simultaneous acquisition of image and navigator slices using CAIPIRINHA for 4D MRI *Magn. Reson. Med.* **73** 669–76
- Chan R W, Ramsay E A, Cunningham C H and Plewes D B 2009 Temporal stability of adaptive 3D radial MRI using multidimensional golden means *Magn. Reson. Med.* **61** 354–63
- Chandarana H, Feng L, Ream J, Wang A, Babb J S, Block K T, Sodickson D K and Otazo R 2015 Respiratory motion-resolved compressed sensing reconstruction of free-breathing radial acquisition for dynamic liver magnetic resonance imaging *Invest. Radiol.* **50** 749–56
- Deng Z, Pang J, Yang W, Yue Y, Sharif B, Tuli R, Li D, Fraass B and Fan Z 2016 Four-dimensional MRI using three-dimensional radial sampling with respiratory self-gating to characterize temporal phase-resolved respiratory motion in the abdomen *Magn. Reson. Med.* **75** 1574–85
- Deng Z, Yang W, Pang J, Bi X, Tuli R, Li D and Fan Z 2017 Improved vessel-tissue contrast and image quality in 3D radial sampling-based 4D-MRI *J. Appl. Clin. Med. Phys.* **18** 250–7
- Dinkel J, Hintze C, Tetzlaff R, Huber P E, Herfarth K, Debus J, Kauczor H U and Thieke C 2009 4D-MRI analysis of lung tumor motion in patients with hemidiaphragmatic paralysis *Radiother. Oncol.* **91** 449–54
- Dirix P, Haustermans K and Vandecaveye V 2014 The value of magnetic resonance imaging for radiotherapy planning *Semin. Radiat. Oncol.* **24** 151–9
- Du D, Caruthers S D, Glide-hurst C, Low D A, Li H H, Mutic S and Hu Y 2015 High-quality T2-weighted 4-dimensional magnetic resonance imaging for radiation therapy applications *Int. J. Radiat. Oncol. Biol. Phys.* **92** 430–7
- Ehman R L and Felmlee J P 1989 Adaptive technique for high-definition MR imaging of moving structures *Radiology* **173** 255–63
- Engelsman M, Sharp G C, Bortfeld T, Onimaru R and Shirato H 2005 How much margin reduction is possible through gating or breath hold? *Phys. Med. Biol.* **50** 477–90
- Fallone B G 2014 The Rotating Biplanar Linac-Magnetic Resonance Imaging System *Semin. Radiat. Oncol.* **24** 200–2
- Fayad H, Schmidt H, Küstner T and Visvikis D 2017 4-Dimensional MRI and attenuation map generation in PET/MRI with 4-dimensional PET-derived deformation matrices: study of feasibility for lung cancer applications *J. Nucl. Med.* **58** 833–9
- Feng L, Axel L, Chandarana H, Block K T, Sodickson D K and Otazo R 2016 XD-GRASP: golden-angle radial MRI with reconstruction of extra motion-state dimensions using compressed sensing *Magn. Reson. Med.* **75** 775–88
- Feng M, Balter J M, Normolle D, Adusumilli S, Cao Y, Chenvert T L and Ben-josef E 2009 Characterization of pancreatic tumor motion using cine-mri: surrogates for tumor position should be used with caution *Int. J. Radiat. Oncol. Biol. Phys.* **74** 884–91
- Fessler J A, Member S and Sutton B P 2003 Nonuniform Fast Fourier Transforms Using Min-Max Interpolation *IEEE Trans. Signal Process.* **51** 560–74
- Fitzpatrick M J, Starkschall G, Antolak J A, Fu J, Shukla H, Keall P J, Klahr P and Mohan R 2005 Displacement-based binning of time-dependent computed tomography image data sets *Med. Phys.* **33** 235–46
- Freedman J N, Collins D J, Bainbridge H, Rank C M, Nill S, Kachelrieß M, Oelfke U, Leach M O and Wetscherek A 2017 T2-Weighted 4D magnetic resonance imaging for application in magnetic resonance-guided radiotherapy treatment planning *Invest. Radiol.* **52** 563–73
- Glide-Hurst C K, Kim J P, To D, Hu Y, Kadbi M, Nielsen T and Chetty I J 2015 Four dimensional magnetic resonance imaging optimization and implementation for magnetic resonance imaging simulation *Pract. Radiat. Oncol.* **5** 433–42
- Glitzner M, de Senneville B D, Lagendijk J J W, Raaymakers B W and Crijs S P M 2015 On-line 3D motion estimation using low resolution MRI *Phys. Med. Biol.* **60** N301–10

- Goldstein S, Ford E, Duhon M, McNutt T, Wong J and Herman J 2010 Use of respiratory-correlated 4dct to determine acceptable treatment margins for locally advanced pancreatic adenocarcinoma *Int. J. Radiat. Oncol. Biol. Phys.* **76** 597–602
- Griswold M A, Jakob P M, Heidemann R M, Nittka M, Jellus V, Wang J, Kiefer B and Haase A 2002 Generalized autocalibrating partially parallel acquisitions (GRAPPA) *Magn. Reson. Med.* **47** 1202–10
- Haacke E M, Brown R W, Thompson M R and Venkatesan R 1999 *Magnetic Resonance Imaging* (New York: Wiley)
- Hammernik K, Klatzer T, Kobler E, Recht M P, Sodickson D K, Pock T and Knoll F 2018 Learning a variational network for reconstruction of accelerated MRI data *Magn. Reson. Med.* **79** 3055–71
- Han F, Zhou Z, Cao M, Yang Y, Sheng K and Hu P 2017 Respiratory motion-resolved, self-gated 4D-MRI using rotating cartesian *k*-space (ROCK) *Med. Phys.* **44** 1359–68
- Han Y, Yoo J, Kim H H, Shin H J, Sung K and Ye J C 2018 Deep learning with domain adaptation for accelerated projection-reconstruction MR *Magn. Reson. Med.* **80** 1189–205
- Harris W, Ren L, Cai J, Zhang Y, Chang Z and Yin F-F 2016 A technique for generating volumetric cine MRI (VC-MRI) *Int. J. Radiat. Oncol.* **95** 844–53
- Harris W, Yin F F, Wang C, Zhang Y, Cai J and Ren L 2018 Accelerating volumetric cine MRI (VC-MRI) using undersampling for real-time 3D target localization/tracking in radiation therapy: a feasibility study *Phys. Med. Biol.* **63** 01NT01
- Heerkens H D, van Vulpen M, van den Berg C A T, Tijssen R H N, Crijns S P M, Molenaar I Q, van Santvoort H C, Reerink O and Meijer G J 2014 MRI-based tumor motion characterization and gating schemes for radiation therapy of pancreatic cancer *Radiother. Oncol.* **111** 252–7
- Hu Y, Caruthers S D, Low D A, Parikh P J and Mutic S 2013 Respiratory amplitude guided 4-dimensional magnetic resonance imaging *Int. J. Radiat. Oncol. Biol. Phys.* **86** 198–204
- Hui C, Wen Z, Stemkens B, Tijssen R H N, van den Berg C A T, Hwang K-P and Beddar S 2016 4D MR imaging using robust internal respiratory signal *Phys. Med. Biol.* **61** 3472–87
- Hyun C M, Kim H P, Lee S M, Lee S and Seo J K 2018 Deep learning for undersampled MRI reconstruction *Phys. Med. Biol.* **63** 135007
- International Commission on Radiation Units and Measurements 1999 Prescribing, recording, and reporting photon beam therapy *ICRU Report 62* (supplement to ICRU report 50) (<https://doi.org/10.1093/jicru/ndx010>)
- Kauczor H U and Plathow C 2006 Imaging tumour motion for radiotherapy planning using MRI *Cancer Imaging* **6** 140–4
- Keall P J, Barton M and Crozier S 2014 The Australian Magnetic Resonance Imaging-Linac Program *Semin. Radiat. Oncol.* **24** 203–6
- Kim S G, Feng L, Grimm R, Freed M, Block K T, Sodickson D K, Moy L and Otazo R 2016 Influence of temporal regularization and radial undersampling factor on compressed sensing reconstruction in dynamic contrast enhanced MRI of the breast *J. Magn. Reson. Imaging* **43** 261–9
- Kontaxis C, Bol G H, Lagendijk J J W and Raaymakers B W 2015 A new methodology for inter- and intrafraction plan adaptation for the MR-linac *Phys. Med. Biol.* **60** 7485–97
- Kontaxis C, Bol G H, Stemkens B, Glitzner M, Prins F M, Kerkmeijer L G W, Lagendijk J J W and Raaymakers B W 2017 Towards fast online intrafraction replanning for free-breathing stereotactic body radiation therapy with the MR-linac *Phys. Med. Biol.* **62** 7233–48
- Küstner T et al 2017 Self-navigated 4D cartesian imaging of periodic motion in the body trunk using partial *k*-space compressed sensing *Magn. Reson. Med.* **78** 632–44
- Lagendijk J J W, van Vulpen M and Raaymakers B W 2016 The development of the MRI linac system for online MRI-guided radiotherapy: a clinical update *J. Intern. Med.* **280** 203–8
- Li G, Wei J, Olek D, Kadbi M, Tyagi N, Zakian K, Mechalakos J, Deasy J O and Hunt M 2017 Direct comparison of respiration-correlated four-dimensional magnetic resonance imaging (4DMRI) reconstructed based on concurrent internal navigator and external bellows *Int. J. Radiat. Oncol.* **97** 596–605
- Liang X, Yin F-F, Liu Y and Cai J 2016 A probability-based multi-cycle sorting method for 4D-MRI: a simulation study *Med. Phys.* **43** 6375–85
- Liu J and Saloner D 2014 Accelerated MRI with circular Cartesian undersampling (CIRCUS): a variable density Cartesian sampling strategy for compressed sensing and parallel imaging *Quantum Imaging Med. Surg.* **4** 57–67
- Liu Y, Yin F, Chen N, Chu M, Cai J, Liu Y, Yin F and Chen N 2015b Four dimensional magnetic resonance imaging with retrospective *k*-space reordering: a feasibility study *Med. Phys.* **42** 534–41
- Liu Y, Yin F, Rhee D and Cai J 2016 Accuracy of respiratory motion measurement of 4D-MRI: A comparison between cine and sequential acquisition *Med. Phys.* **43** 179–87
- Liu Y, Yin F-F, Chang Z, Czito B G, Palta M, Bashir M R, Qin Y and Cai J 2014 Investigation of sagittal image acquisition for 4D-MRI with body area as respiratory surrogate *Med. Phys.* **41** 101902
- Liu Y, Yin F-F, Czito B G, Bashir M R and Cai J 2015a T2-weighted four dimensional magnetic resonance imaging with result-driven phase sorting *Med. Phys.* **42** 4460–71
- Liu Y, Yin F-F, Czito B G, Bashir M R, Palta M and Cai J 2017a Retrospective four-dimensional magnetic resonance imaging with image-based respiratory surrogate: a sagittal-coronal-diaphragm point of intersection motion tracking method *J. Med. Imaging* **4** 024007
- Liu Y, Zhong X, Czito B G, Palta M, Bashir M R, Dale B M, Yin F F and Cai J 2017b Four-dimensional diffusion-weighted MR imaging (4D-DWI): a feasibility study *Med. Phys.* **44** 397–406
- Lu W, Parikh P J, Hubenschmidt J P, Bradley J D and Low D A 2006 A comparison between amplitude sorting and phase-angle sorting using external respiratory measurement for 4D CT *Med. Phys.* **33** 2964
- Lujan A E, Larsen E W, Balter J M and Ten Haken R K 1999 A method for incorporating organ motion due to breathing into 3D dose calculations *Med. Phys.* **26** 715–20
- Lustig M, Donoho D and Pauly J M 2007 Sparse MRI: the application of compressed sensing for rapid MR imaging *Magn. Reson. Med.* **58** 1182–95
- Marx M, Ehrhardt J, Werner R, Schlemmer H P and Handels H 2014 Simulation of spatiotemporal CT data sets using a 4D MRI-based lung motion model *Int. J. Comput. Assist. Radiol. Surg.* **9** 401–9
- Masuda Y and Haneishi H 2010 4D MR imaging of respiratory organ motion using an intersection profile method *SPIE Med. Imaging* **7625** 76250Z
- McWilliam A, Kennedy J, Hodgson C, Vasquez Osorio E, Faivre-Finn C and van Herk M 2017 Radiation dose to heart base linked with poorer survival in lung cancer patients *Eur. J. Cancer* **85** 106–13
- Ménard C and van der Heide U A 2014 Introduction: magnetic resonance imaging comes of age in radiation oncology *Semin. Radiat. Oncol.* **24** 149–50
- Mickevicius N J and Paulson E 2017 Investigation of undersampling and reconstruction algorithm dependence on respiratory correlated 4D-MRI for online MR-guided radiation therapy *Phys. Med. Biol.* **62** 2910–21
- Miller K L 2012 FMRI using balanced steady-state free precession (SSFP) *NeuroImage* **62** 713–9

- Mutic S and Dempsey J F 2014 The ViewRay system: magnetic resonance-guided and controlled radiotherapy *Semin. Radiat. Oncol.* **24** 196–9
- Nayak K S, Hargreaves B A, Hu B S, Nishimura D G, Pauly J M and Meyer C H 2005 Spiral balanced steady-state free precession cardiac imaging *Magn. Reson. Med.* **53** 1468–73
- Nehrke K and Manke D 2000 Advanced Navigator Techniques *Int. J. Bioelectromagn.* **2** 1–7
- Paganelli C, Lee D, Kipritidis J, Whelan B, Greer P B, Baroni G, Riboldi M and Keall P 2018 Feasibility study on 3D image reconstruction from 2D orthogonal cine-MRI for MRI-guided radiotherapy *J. Med. Imaging Radiat. Oncol.* **62** 389–400
- Paganelli C, Summers P, Bellomi M, Baroni G and Riboldi M 2015 Liver 4DMRI: A retrospective image-based sorting method *Med. Phys.* **42** 4814–21
- Park J, Shin T, Yoon S H, Goo J M and Park J-Y 2016 A radial sampling strategy for uniform k-space coverage with retrospective respiratory gating in 3D ultrashort-echo-time lung imaging *NMR Biomed.* **29** 576–87
- Park S, Farah R, Shea S M, Tryggestad E, Hales R and Lee J 2018 Simultaneous tumor and surrogate motion tracking with dynamic MRI for radiation therapy planning *Phys. Med. Biol.* **63** 025015
- Pickles M D, Gibbs P, Sreenivas M and Turnbull L W 2006 Diffusion-weighted imaging of normal and malignant prostate tissue at 30 T *J. Magn. Reson. Imaging* **23** 130–4
- Plathow C, Meinzer H-P and Kauczor H-U 2006 MRT-Analyse der Bewegungen von Lungenrundherden *Radiologe* **46** 260–6
- Plathow C, Schoebinger M, Fink C, Ley S, Puderbach M, Eichinger M, Bock M, Meinzer H-P and Kauczor H-U 2005 Evaluation of lung volumetry using dynamic three-dimensional magnetic resonance imaging *Invest. Radiol.* **40** 173–9
- Pruessmann K P, Weiger M, Börner P and Boesiger P 2001 Advances in sensitivity encoding with arbitrary k-space trajectories *Magn. Reson. Med.* **46** 638–51
- Pruessmann K P, Weiger M, Scheidegger M B and Boesiger P 1999 SENSE: sensitivity encoding for fast MRI *Magn. Reson. Med.* **42** 952–62
- Qin C, Schlemper J, Caballero J, Price A, Hajnal J V and Rueckert D 2017 *Convolutional Recurrent Neural Networks for Dynamic MR Image Reconstruction* (arXiv:1712.01751v3)
- Rank C M, Heuber T, Brehm M and Kachelrieß M 2016a Artifact model-based respiratory motion compensation (MoCo) for simultaneous PET/MR based on strongly undersampled radial MR data 2014 *IEEE Nuclear Science Symp. and Medical Imaging Conf. (NSS/MIC)* (Seattle, WA, USA, 8–15 November 2014) (*IEEE*) **43** 6234–45
- Rank C M, Heußer T, Buzan M T A, Wetscherek A, Freitag M T, Dinkel J and Kachelrieß M 2017 4D Respiratory Motion-Compensated Image Reconstruction of Free-Breathing Radial MR Data with Very High Undersampling *Magn. Reson. Med.* **77** 1170–83
- Rank C M, Heußer T, Wetscherek A and Kachelrieß M 2016b Respiratory motion compensation for simultaneous PET/MR based on strongly undersampled radial MR data *Med. Phys.* **43** 6234–45
- Remmert G, Biederer J, Lohberger F, Fabel M and Hartmann G H 2007 Four-dimensional magnetic resonance imaging for the determination of tumour movement and its evaluation using a dynamic porcine lung phantom *Phys. Med. Biol.* **52** N401–15
- Rietzel E, Pan T and Chen G T 2005 Four-dimensional computed tomography: image formation and clinical protocol *Med. Phys.* **32** 874–89
- Roemer P B, Edelstein W A, Hayes C E, Souza S P and Mueller O M 1990 The NMR phased array *Magn. Reson. Med.* **16** 192–225
- Rohlfing T, Maurer C R, O'Dell W G and Zhong J 2004 Modeling liver motion and deformation during the respiratory cycle using intensity-based nonrigid registration of gated MR images *Med. Phys.* **31** 427–32
- Roujou S, Ries M, Moonen C and De Senneville B D 2011 Automatic non-rigid calibration of image registration for real time interventional MRI of mobile organs *IEEE Trans. Med. Imaging* **30** 1737–45
- Scheffler K 1999 A pictorial description of steady-state in rapid magnetic resonance imaging *Concepts Magn. Reson.* **11** 291–304
- Scheffler K and Lehnhardt S 2003 Principles and applications of balanced SSFP techniques *Eur. Radiol.* **13** 2409–18
- Sodickson D K and Manning W J 1997 Simultaneous acquisition of spatial harmonics (SMASH): fast imaging with radiofrequency coil arrays *Magn. Reson. Med.* **38** 591–603
- Stemkens B et al 2017b Effect of intra-fraction motion on the accumulated dose for free-breathing MR-guided stereotactic body radiation therapy of renal-cell carcinoma *Phys. Med. Biol.* **62** 7407–24
- Stemkens B, Van Den Berg C A T, Bruijnen T, Prins F and Kerkmeijer L 2017a A dual-purpose MR acquisition for combined 4D-MRI and dynamic contrast enhanced imaging *59th AAPM*
- Stemkens B, Sbrizzi A, Andreychenko A A, Crijs S P M, Lagendijk J J W, Van den Berg C A T and Tijssen R H N 2016a An optimization framework to maximize signal-to-noise ratio in simultaneous multi-slice body imaging *NMR Biomed.* **29** 275–83
- Stemkens B, Tijssen R H N, de Senneville B D, Lagendijk J J W and van den Berg C A T 2016b Image-driven, model-based 3D abdominal motion estimation for MR-guided radiotherapy *Phys. Med. Biol.* **61** 5335–55
- Stemkens B, Tijssen R H N, Denis de Senneville B, Heerkens H D, Van Vulpen M, Lagendijk J J W and van den Berg C A T 2015 Optimizing 4-dimensional magnetic resonance imaging data sampling for respiratory motion analysis of pancreatic tumors *Int. J. Radiat. Oncol. Biol. Phys.* **91** 571–8
- Stemkens B, Tijssen R H N, van den Berg C A T, Lagendijk J J W, Moonen C T W, Ries M and de Senneville B D 2013 Optical flow analysis on undersampled radial acquisitions for real-time tracking of the pancreas in MR guided radiotherapy *Proc. Int. Soc. Magn. Reson. Med.* **21** 4325
- Swastika W, Masuda Y, Xu R, Kido S, Chen Y-W and Haneishi H 2013 GND-PCA-based statistical modeling of diaphragm motion extracted from 4D MRI *Comput. Math. Methods Med.* **2013** 482941
- Tai A, Liang Z, Erickson B and Li X A 2013 Management of respiration-induced motion with 4-dimensional computed tomography (4DCT) for pancreas irradiation *Int. J. Radiat. Oncol. Biol. Phys.* **86** 908–13
- Tanner C, Samei G and Székely G 2014 Improved reconstruction of 4D-MR images by motion predictions *MICCAI* pp 146–53
- To D T, Kim J P, Price R G, Chetty I J and Glide-Hurst C K 2016 Impact of incorporating visual biofeedback in 4D MRI *J. Appl. Clin. Med. Phys.* **17** 128–37
- Tokuda J, Morikawa S, Haque H A, Tsukamoto T, Matsumiya K, Liao H, Masamune K and Dohi T 2008 Adaptive 4D MR imaging using navigator-based respiratory signal for MRI-guided therapy *Magn. Reson. Med.* **59** 1051–61
- Tong Y, Udupa J K, Ciesielski K C, McDonough J M, Mong A and Campbell R M 2014 Graph-based retrospective 4D image construction from free-breathing MRI slice acquisitions *Proc. SPIE* **9038** 90380I
- Tong Y, Udupa J K, Ciesielski K C, Wu C, McDonough J M, Mong D A and Campbell R M 2017 Retrospective 4D MR image construction from free-breathing slice acquisitions: a novel graph-based approach *Med. Image Anal.* **35** 345–59
- Tryggestad E, Flammang A, Han-Oh S, Hales R, Herman J, McNutt T, Roland T, Shea S M and Wong J 2013 Respiration-based sorting of dynamic MRI to derive representative 4D-MRI for radiotherapy planning *Med. Phys.* **40** 51909
- Uh J, Khan M A and Hua C 2016 Four-dimensional MRI using an internal respiratory surrogate derived by dimensionality reduction *Phys. Med. Biol.* **61** 7812–32

- Uh J, Krasin M J, Li Y, Li X, Tinkle C, Lucas J T, Merchant T E and Hua C 2017 Quantification of pediatric abdominal organ motion with a 4-dimensional magnetic resonance imaging method *Int. J. Radiat. Oncol.* **99** 227–37
- Unkelbach J and Oelfke U 2004 Inclusion of organ movements in IMRT treatment planning via inverse planning based on probability distributions *Phys. Med. Biol.* **49** 4005–29
- van de Lindt T N, Schubert G, van der Heide U A and Sonke J-J 2016 An MRI-based mid-ventilation approach for radiotherapy of the liver *Radiother. Oncol.* **121** 276–80
- van der Heide U A, Houweling A C, Groenendaal G, Beets-Tan R G H and Lambin P 2012 Functional MRI for radiotherapy dose painting *Magn. Reson. Imaging* **30** 1216–23
- von Siebenthal M, Cattin P, Gamper U, Lomax A and Székely G 2005 4D MR imaging using internal respiratory gating *Med. Image Comput. Assist. Interv.* **8** 336–43
- Von Siebenthal M, Székely G, Gamper U, Boesiger P, Lomax A and Cattin P 2007 4D MR imaging of respiratory organ motion and its variability *Phys. Med. Biol.* **52** 1547
- Watkins W T, Li R, Lewis J, Park J C, Sandhu A, Jiang S B and Song W Y 2010 Patient-specific motion artifacts in 4DCT *Med. Phys.* **37** 2855–61
- Wink N, Panknin C and Solberg T D 2006 Phase versus amplitude sorting of 4D-CT data *J. Appl. Clin. Med. Phys.* **7** 77–85
- Winkelmann S, Schaeffter T, Koehler T, Eggers H and Doessel O 2007 An optimal radial profile order based on the Golden Ratio for time-resolved MRI *IEEE Trans. Med. Imaging* **26** 68–76
- Wolthaus J W H, Schneider C, Sonke J-J, van Herk M, Belderbos J S A, Rossi M M G, Lebesque J V and Damen E M F 2006 Mid-ventilation CT scan construction from four-dimensional respiration-correlated CT scans for radiotherapy planning of lung cancer patients *Int. J. Radiat. Oncol.* **65** 1560–71
- Wolthaus J W H, Sonke J J, Van Herk M and Damen E M F 2008b Reconstruction of a time-averaged midposition CT scan for radiotherapy planning of lung cancer patients using deformable registration *Med. Phys.* **35** 3998–4011
- Wolthaus J W H, Sonke J-J, van Herk M, Belderbos J S A, Rossi M M G, Lebesque J V and Damen E M F 2008a Comparison of different strategies to use four-dimensional computed tomography in treatment planning for lung cancer patients *Int. J. Radiat. Oncol. Biol. Phys.* **70** 1229–38
- Würslein C, Schmidt H, Martirosian P, Brendle C, Boss A, Schwenzer N F and Stegger L 2013 Respiratory motion correction in oncologic PET using T1-weighted MR imaging on a simultaneous whole-body PET/MR system *J. Nucl. Med.* **54** 464–71
- Yamamoto T, Langner U, Loo B W Jr, Shen J and Keall P J 2008 Retrospective analysis of artifacts in four-dimensional CT images of 50 abdominal and thoracic radiotherapy patients *Int. J. Radiat. Oncol. Biol. Phys.* **72** 1250–8
- Yang J, Cai J, Wang H, Chang Z, Czito B G, Bashir M R and Yin F-F 2014 Four-dimensional magnetic resonance imaging using axial body area as respiratory surrogate: initial patient results *Int. J. Radiat. Oncol. Biol. Phys.* **88** 907–12
- Yang J, Wang H, Yin Y and Li D 2015a Reducing motion artifacts in 4D MR images using principal component analysis (PCA) combined with linear polynomial fitting model *J. Appl. Clin. Med. Phys.* **16** 144–60
- Yang P C, Kerr A B, Liu A C, Liang D H, Hardy C, Meyer C H, Macovski A, Pauly J M and Hu B S 1998 New real-time interactive cardiac magnetic resonance imaging system complements echocardiography *J. Am. Coll. Cardiol.* **32** 2049–56
- Yang W, Fan Z, Tuli R, Deng Z, Pang J, Wachsman A, Reznik R, Sandler H M, Li D and Fraass B A 2015c Four dimensional magnetic resonance imaging with 3D radial sampling and self-gating based K -space sorting: early clinical experience on pancreatic cancer patients *Int. J. Radiat. Oncol.* **93** S19
- Yang W, Fan Z, Tuli R, Deng Z, Pang J, Wachsman A, Reznik R, Sandler H, Li D and Fraass B A 2015b Four-dimensional magnetic resonance imaging With 3-dimensional radial sampling and self-gating-based K -space sorting: early clinical experience on pancreatic cancer patients *Int. J. Radiat. Oncol. Biol. Phys.* **93** 1136–43
- Yang Y X, Teo S-K, Van Reeth E, Tan C H, Tham I W K and Poh C L 2015d A hybrid approach for fusing 4D-MRI temporal information with 3D-CT for the study of lung and lung tumor motion *Med. Phys.* **42** 4484–96
- Yue Y, Fan Z, Yang W, Pang J, Deng Z and McKenzie E 2015a Geometric validation of k -space self-gated 4D-MRI versus 4D-CT using a respiratory motion phantom *Med. Phys.* **42** 5787–97
- Yue Y, Fan Z, Yang W, Pang J, Deng Z, McKenzie E, Tuli R, Wallace R, Li D and Fraass B 2015b Geometric validation of self-gating k -space-sorted 4D-MRI versus 4D-CT using a respiratory motion phantom *Med. Phys.* **42** 5787